UNIVERSITA' DEGLI STUDI DI NAPOLI "FEDERICO II"

DEPARTMENT OF CHEMICAL, MATERIALS AND PRODUCTION ENGINEERING

(DICMAPI)

PHD IN "INDUSTRIAL PRODUCT AND PROCESS ENGINEERING", XXXIV CYCLE

"WIDE-RANGE COMPRESSION FORCES TO INVESTIGATE SINGLE-CELL IN-FLOW MOTIONS, MECHANOBIOLOGICAL RESPONSES AND INTRACELLULAR DELIVERY."

Coordinator

Ch.mo Prof. Andrea D'Anna

Scientific Committee

David Dannhauser, Ph.D.

Supervisor   **Author**

Ch.mo Prof. Filippo Causa   Maria Isabella Maremonti

Ch.mo Paolo Antonio Netti

November 2018 – November 2021

Index

Acknowledgments

I would like to express my deepest gratitude to all those who have supported me in this work.

In particular, I would like to thank *Prof. Filippo Causa* and *Prof. Paolo Antonio Netti* for giving me the opportunity to join their research group and work with beautiful people.

The encouragement, guidance and support of *David Dannhauser* and *Valeria Panzetta* enabled me to produce such a satisfying research work. They gave me valuable tools and knowledge without which experience would not be the same. Like research, like personal life.

In addition, discussions and collaborations with all *my colleagues* have contributed substantially to this work. Thank you all.

Without the great support of *my family* and *friends*, old and new, nothing would have been the same. To each of them, I dedicate a part of this beautiful experience.

Finally, I dedicate this work to *Massi*, the most beautiful surprise of these years. He took me by the hand and accompanied me, always.

Abstract

The aim of the PhD work is to create a new microfluidic approach to finely tune applied in-flow forces in order to explore controlled single-cell deformation. In fact, we propose a microfluidic device based on compression forces arising from a viscoelastic fluid solution that firstly align cells and then deform them. By simply changing the rheological properties and the imposed fluid-flow conditions, our approach represents an easy-to-use and versatile tool to collect a comprehensive mapping of single-cell properties, investigating both biophysical and biomechanical characteristics. In a wide-range of applied compression, we observe how different degrees of deformation lead to cell-specific deformation-dependent in-flow dynamics, which correlate the classical deformation parameters (e.g. cell aspect-ratio), with dynamic quantities (e.g. revolution time of rotation during in-flow motion). Thus, a precise in-flow label-free cell phenotyping is achieved allowing the distinction of different cell classes. The observation of different degrees of deformation corresponding to variable compression, lead us to interrogate the inner cell structures possibly involved into the mechanical responses. We demonstrate that re-organization phenomena of actin cortex and microtubules as well as of nuclear envelope and chromatin content, occur. Also in this case, cell-specific responses are collected, allowing us to distinguish healthy from pathological cells depending on the structural mechanical reaction. Furthermore, by playing with the high levels of compression, we show preliminary results about the possibility to induce a nanoparticle intracellular delivery process by escaping physiological endocytosis. In fact, cells result to be able to incorporate nanoparticles into the cytoplasm, without involving a vesicle formation for the entry. These

outcome open up new interesting scenarios about the possibility to use the microfluidic device as a platform for cell phenotyping and intracellular delivery, properly engineered for both diagnostic and therapeutic purposes.

List of abbreviations

Viscoelastic compressive force	F_{EMax}
Nuclear Envelope	*NE*
Nuclear Pore Complexes	*NPCs*
Yes-associated Protein	*YAP*
cyclic GMP-AMP synthase	*cGAS*
Contraction ratio	*CR*
Aspect ratio	*AR*
Reynold's number	*Re*
Weissenberg number	*Wi*
Elasticity number	*El*
Cell deformation	*CD*
Nucleus/Cytoplasmic ratio	*Nucl/Cyt ratio*
Chromatin condensation parameter	*CCP*
Nanoparticles	*NPs*

Polyethylene oxide   *PEO*

Quiescent measurement   *Q, Control, CTRL*

In-flow measurement in Section B T_B

In-flow measurement in Section D T_D

Quiescent measurement of after in-flow T_E, *PEO 05, PEO 09*
cell deformation

Cytochalasin D   *CYTD*

Nocodazole   *NOCO*

x

1. Introduction

Cells are able to sense both biochemical and physical cues, such as forces, geometry and substrate rigidity. These factors play a critical role in defining cell functions, morphology and state. Mechanobiology studies how these biochemical and physical factors influence the physiological cell processes of cell mechanotransduction and mechanosensing [1]. The former describes the intracellular molecular processes through which external cues are transformed into biological and biochemical responses as adaptation of the cell to the dynamic modifications of the microenvironment. Differently, mechanosensing defines the ability of cells to sense forces and physical stimuli by changing the inner protein conformation (e.g. cytoskeletal components) which in turns affects cell shape and motility [1,2]. Then, how cells respond to applied external forces strongly depends on the inner cell compartments that are involved in the deformation reaction. In general, the deformability of cells represents a powerful label-free biomarker underlying cytoskeletal and nuclear mechanical changes indicative of pathological or healthy cell states [3]. For instance, increased cell deformability of invasive cancer cells compared to benign ones of the same origin, or alterations in stiffness of leukocytes in response to activation pathways can be studied. In this context, high-throughput, rapid and low-cost analysis techniques are required to assess deformability properties of cells in order to achieve precise phenotyping outcome for cell classification. However, as cells are highly heterogeneous, the magnitude of force and the time of application to deform them, strongly influence the final phenotype outcome [4]. Up to now, mechanical cell properties have been fully characterized by viscoelasticity

theory, addressing detailed information of imposed mechanical load entity and time-scales. Thus, the cell response to external loads is driven by both, an active and a passive intrinsic cell remodelling of cytoskeletal contents and various organelles. Depending on whether forces apply local deformation, stretching or compression, cells respond mechanically in distinct ways, since the internal structures are stressed differently [4-6]. Particularly, it has been demonstrated that for small deformation (~pN) and long times of stress applications (~min), the major contribution in suspended cell response is caused by the actin cortex that, underlying the plasma membrane, shows a passive elastic behaviour [6,7]. On the contrary, at large deformation and relatively low time scales (from ms to s), actin cortex components do not play a relevant role because they tend to disrupt, and the microtubule network and the nucleus contribution become dominant in the opposing to the applied load [6-8]. Particularly, cell nucleus plays a central role in mechanosensing processes with related changes in nuclear envelope (NE) composition, mainly constituted by the Lamin A/C and the Nuclear Pore Complexes (NPCs), both deputed to finely tune chromatin re-organization - in the sense of condensation- and to regulate the trafficking of different re-localizing molecules. In details, the Lamin A/C network provides a structural support and governs nuclear deformability and fragility. High Lamin A/C expression levels are referred to stiffer and more viscous nuclei, whereas a deficiency of Lamin A/C correlates to both more deformable and fragile nuclei, leading to possible nuclear breakage and cell death [9-11]. In adhesive conditions, thanks to a well-structured cytoskeleton, Lamin A/C expression and conformation have been detected to be directly involved in mechanosensing and mechanotransduction processes [12-15]. In fact, the activation of production and/or recycling processes of Lamin A/C resulted

2

to be closely regulated by human tissue-mimicking substrate stiffnesses. Similarly, the translocation of Yes-associated Protein (YAP) transcription factor into the nucleus represents a typical mechanosensing phenomenon, observed during cell adhesion or migration -once the cytoskeleton is assembled- as a consequence of a signalling cascade coming from the imposed mechanical stimulus like a variable substrate stiffness [13-16]. However, the transient influx of cytoplasmic proteins into the nucleus (e.g. YAP) as well as the accumulation of DNA to cyclic GMP-AMP synthase (cGAS) factor at the cytosolic side of the nucleus are processes that can be ascribable also to Lamin A/C structural ruptures due to the effects of a cell migration into strict geometrical constrictions or cytoskeletal tensions acting on the nucleus [17]. Thus, both compressive and tensile forces can cause ruptures of the Lamin A/C, inducing an enhanced exposure of the nuclear content to the cytoplasm and possible DNA damages [18,19]. In fact, diffusion experiments of macromolecules into the cell nucleus reveal that their movement can be affected by viscosity, active transport, or the presence of obstacles such as the Lamin A/C structure and chromatin condensation, as well as by their dimension and molecular weight [20-22]. This implies that the application of an external force on the cell nucleus and its consequent deformation could favour molecule trafficking across the NE. In quasi-suspended cells, it was demonstrated that forces directly applied up to the nucleus level contribute to a nuclear YAP translocation, by decreasing the NE mechanical resistance, regardless the formation of a well-structured cell cytoskeleton. In fact, nuclear flattening can cause a NPCs stretching [23].

During the past decade, mechanical studies of cells and their own subcellular components have rapidly evolved. In fact, different techniques

are employed to induce cell deformation, reducing the costs and yielding improved repeatability for classifying cells [8]. The different approaches can be divided into two main classes, the first regarding the possibility to perform a single cell analysis and the second based on microfluidic alternatives to investigate multiple cells. In general, micromanipulation techniques based on magnetic, optical, and mechanical means considerably improved a precise probing of cellular structures to study their responses [4,8]. Below, we list some of the techniques employed to perform single cell analysis, manipulating and measuring the mechanical properties of living cells (Fig. 1). Notice that, such techniques are time-consuming processes, since they work on just one cell per time, acquiring the relevant parameters.

- In **Atomic force microscopy** (AFM), a sharp tip at the free end of a flexible cantilever generates a local deformation on the cell surface (Fig. 1a).The resulting deflection of the cantilever tip can be calibrated to estimate the applied force, generally ranging from 10^{-6} to 10^{-2} N [4,5].

- **Micropipette aspiration** is a classical technique for quantifying the mechanical properties of individual cells, such as elastic modulus and viscosity (Fig. 1c). The technique applies a negative pressure to deform cells, which elongate into a portion of the micropipette. The resulting aspiration length varies with the applied pressure. A glass micropipette with an internal diameter of 1–5 μm is typically used. The micropipette is moved by a micromanipulator to contact a cell. Vacuum is applied through the micropipette to the cell. The aspiration pressures are typically on the order of 1 pNμm^{-2} = 1 Pa for soft cells and 1 nNμm^{-2} = 1 kPa for stiff cells. Then, the corresponding force values required to deform soft cells are on the order of 10–100 pN and several nanonewtons

for stiff cells. The key parameters of such approach include the accuracy of applied pressure, the accuracy of cellular geometrical parameter measurements and the synchronization of applied pressure and resulting geometrical changes of the cell.

- **Optical tweezers** provide an attraction force, created between a dielectric bead of high refractive index and a laser beam, pulling the bead towards the focal point of the trap (Fig. 1f). One typical example of the optical tweezers to deform a single cell, a trap is used with two microbeads attached to the opposite ends of a cell [4].
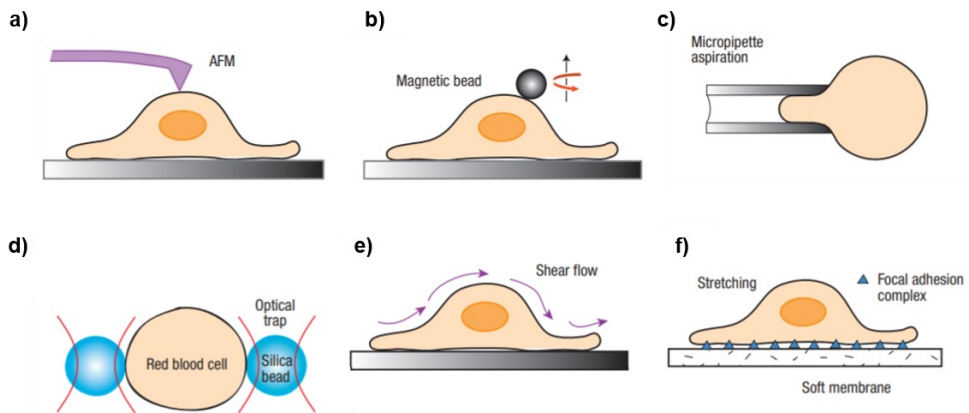

Fig.1 Schematic representation of techniques for characterizing and stimulating single-cells for mechanobiology study [4]. A) Atomic force microscopy (AFM). B) Magnetic twisting cytometry (MTC). c) Micropipette aspiration. D) Optical Trapping. e) Shear flow stretching. F) Micro- and nanotopographic substrate.

- **Shear flow stretching devices** are conceived to impose both laminar and turbulent flows on cells using either cone-and-plate viscometers or parallel-plate flow chambers. In both cases the shear stress applied to cells can be readily quantified (Fig. 1e) [4].

- **Micro- and nanotopographic substrate**. By systematically altering the mechanical properties of the substrate material through changing the degree of crosslink in the polymeric gel, the individual and collective interactions of the cells with the substrate can be studied (Fig. 1f). By using elastic micropatterned substrates, the relationship between force applied by the cell to the substrate and the assembly of focal adhesions can be investigated. The contractile forces generated by cells during locomotion and mitosis have also been measured with a deformable-substrate method [4].

Nowadays, microfluidic approaches allow a totally new perspective in the study of cell mechanics, compared to traditional methods such as AFM or micropipette aspiration. For instance, microfluidics can solve the problem of cell throughput rates (100-10000 cells/sec) as well as enable the possibility to deform cells in hydrodynamic conditions, involving the whole cell structure. In general, the combination of a microfluidic chip with high-speed camera systems allow the direct and rapid measurement of cell dimension, morphology and deformability. Beyond, it offers the unique opportunity to directly measure and detect dynamics and trajectories of deformed objects, in certain fluid-flow conditions [24-28]. Moreover, in-flow dynamics of deformed cells could turn out to be a direct consequence of the obtained cell deformation, becoming an interesting research tool for a label-free single-cell phenotyping. It is well known that the dynamics of red blood cells, regarded as natural spheroidal objects, result to be dramatically governed by the inner rheological and mechanical properties, as internal viscosity and cytoskeletal elasticity [24]. It leads to the possibility of a

backward analysis of cell mechanical properties, such as the shear modulus, using the angle of cell rotation and the respective in-flow variation. Experimental and simulative results in a simple shear flow revealed that the initial orientations of spheroidal objects strongly influence their dynamic behaviours and trajectories [26].

For instance, when the revolution axis of the spheroidal object is in the shear plane, the object can rotate as a *tumbling* motion. Differently, when the long axis of the object oscillates around a mean orientation in the shear plane and the membrane rotates about the spheroidal shape, the object takes a *tank-treading* motion. Another in-flow dynamics is found when the object revolution axis is perpendicular to the shear plane, taking a *rolling* motion [26-29]. Governing factors for such cell motion regimes are i) the imposed velocity field, ii) the chosen fluid rheology, iii) the initial position of the object and iv) its own shape, defined as aspect ratio and, eventually, as cell deformation [27,28]. As result, when objects of different shapes move in a microfluidic chip at the same velocity condition and start from the same initial position, the only significant parameter for the variation of the in-flow dynamics is the shape *per se*. These findings could be used as a new microfluidic tool for the measurement of single-cell mechanical properties.

In general, properly designed microfluidic chips facilitate detection and observation of in-flow dynamics. For example, expansion channel designs allow cell dynamics observations in viscoelastic fluid-flow conditions, leading to an enhanced distinction of the rotation regimes, helping in the analysis of the different behaviours [29,30].

Below, is a list of some examples of microfluidic techniques that are employed to mechanically investigate cells.
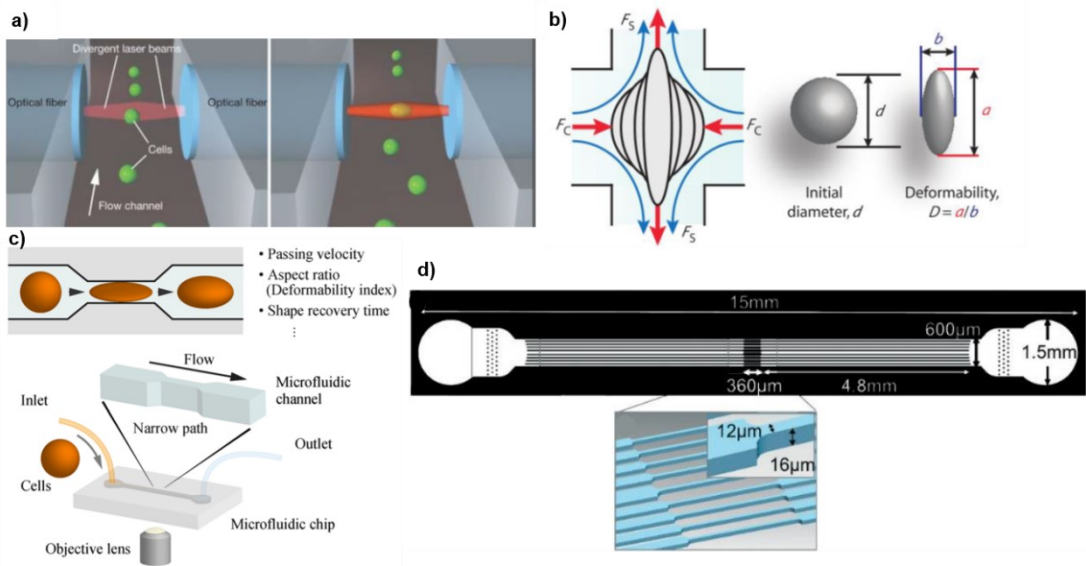
Fig. 2 Microfluidic approaches for whole cell deformation. a) Optical stretcher combined with a microfluidic platform [32]. b) Extensional cell deformation through inertia-driven flow conditions [34]. c) and d) Constriction-based microchannels for whole cell and nuclear mechanical characterization, respectively [32,33].

• An **optical stretcher** combines the use of a microfluidic platform for the cell flow and the application of an external apparatus of laser for cell stretching (Fig. 2a) [30,33].

• **Inertial microfluidics** plays an important role in studying cell deformability. Different geometrical configurations were proposed in last years for focusing, deformation and sorting of cells. When cells are flowing in a fluid with non-negligible inertia, they are affected by an inertial lift force that induces lateral migration of particles toward equilibrium positions between the channel centreline and channel walls [34-38]. Channels with wide sections are employed to deform cells by imposing a fluid-induced deformation, as extensional or shear forces, avoiding any contact between the cells and the channel walls (Fig. 2b) [34,38].

• **Constriction-based microchannels** represent an alternative to the above-mentioned techniques. Regardless of the imposition of an inertial or laminar regime, it is possible to induce deformation by using a microchannel with dimensions comparable or less to those of the cells of interest (Fig. 2c-d). The applied force is a compressive force, coming from the applied pressure difference to push the cell inside the microchannel [12, 39,40].

Major drawbacks of such microfluidic approaches are cell clogging and low throughput. Instead, simple fluid-flow shear forces can deform cells, even though, in this case, a proper calibration and variation of the hydrodynamic force is necessary [41-42]. An interesting possibility to obtain a good calibration and wide application range of deformative forces, according to the chosen flowing fluid and the used channel geometry, is given by **viscoelastic fluids**. In general, when cells move in a viscoelastic solutions, they are influenced by an elastic force (F_E) that guides particle migration thanks to an unbalance of both first and second normal stresses [43]. Due to their intrinsically viscous and elastic features, viscoelastic fluids demonstrate extraordinary physical properties extensively exploitable both as body fluids models or as liquid solution for in-flow particle manipulation. For example, viscoelastic solutions can be used to precisely align cells in-flow to enable single cell analysis approaches [43,44]. Moreover, cells could experience a viscoelasticity induced force, which provokes a deformation useful to separate healthy from pathological cells. Go et al., in 2017, proposed a microfluidic setup constituted by a straight rectangular channel in which normal and hardened red blood cells (RBCs or erythrocytes) moved under the action of a viscoelastic flow . In a Poiseuille flow, cells principally migrate along the centreline of the channel, because of the non-uniform normal stress

distribution that generates the elastic force. By tuning flow rates and shear rates in the channel, Go et al. recorded changes in the deformation degree for normal RBCs, whereas no flow rate effect on the behaviour of hardened cells [45]. Moreover, in rectangular channel sections, the initial orientations of cells could strongly influence their final trajectories, clearly distinguishing different shape-dependent equilibrium positions in-flow [46,47]. Therefore, new design approaches are needed to create a microfluidic chip conceived both for cell deformation and detection of in-flow dynamics. Accordingly, using channels to apply wide ranges of deformative forces and subsequent expansion sections allows cell dynamics observations without further deformation.

The aim of the work is to create a complete mapping of single-cell properties, investigating biophysical and biomechanical characteristics, after the in-flow application of mechanical loading conditions identified as viscoelastic compression forces. Our research question is to identify specific combinations of cell biomarkers, as those for tumoral progression, which can lead to distinct cell signatures outcome for phenotyping. In fact, the main goal is the creation of a rapid, precise and easy-to-use tool for cell phenotyping, in order to directly interrogate single-cell states with the application of in-flow forces at high throughput and with high-resolution methods. Moreover, we study the possibility to enhance translocation phenomena of molecules (e.g. transcription factors) inside the intracellular compartments, as a consequence of the external compression. Here, we present a new microfluidic approach to deform living cells with tuneable compressive forces. We propose to manipulate viscoelastic fluid properties in order to conceive a cell deformation approach based on variable acting

forces, identifying biophysical properties to phenotype cell classes. Our microfluidic chip deforms cells in a contactless and viable way, imposing a wide range of viscoelastic forces (10-$10^3\mu N$). Tuneable forces and relative multiple levels of deformation revealed a precise mechanical phenotyping. In fact, our microfluidic chip has been conceived to classify cell types by deformation-dependent in-flow dynamics, by coupling the classical deformation parameters that describe morphological and shape alterations, with dynamic quantities. We obtain a precise cell type characterization simply based on i) orientation angle, ii) aspect ratio, iii) cell deformation and iv) cell diameter. The combination of this set of parameters leads to a specific mechanical signature of different cell lines and states. Thanks to our highly controlled compressive forces, we investigate cytoskeletal and nuclear responses, as a consequence of cell deformation. We highlight, for suspended cells, the central role of the nucleus in cell deformability. In particular, we demonstrate that, at high cell deformation, nuclear shape alterations occur. Such nuclear deformation can modulate the shuttling of transcription factors, such as YAP (Yes-Associated Protein), and other molecules from the cytoplasm to the nucleus through the nucleo/cytoplasmic barrier. Moreover, the actin cortex constituents and the microtubule networks, as structural components, are of interest to understand their own role in the cell response to the loading condition. We identify different levels of applied loads that generate different deformation responses up to possible structural ruptures events. In the end, we propose to investigate what happens at the level of the cell plasma membrane after deformation. Possible ruptures can occur also at this level, allowing the passage of outer material into the cell, such as functionalized nanoparticles, useful to a single-cell analysis and detection of inner biochemical signals directly inside the cell. In this way, we will be able

to provide a complete characterization of different kinds of cellular biomarkers for rapid and precise diagnosis of physio-pathological states.

2. Material and Methods

2.1. Device concept and fabrication.

We present a novel microfluidic concept for cell deformation in viscoelastic flows (Fig.3). Hereby, cells are guided to move through various consecutive rectangular-shaped sections, by a viscoelastic solution.

Fig. 3 Complete representation of the design concept from the top. Such representation has been extracted from the CAD file project.

The main reason for choosing such a kind of microfluidic concept is the need of a cost-effective, versatile and simple to implement device. However, a pressure-driven flow with negligible inertia is used to guide cells through the microfluidic device. Such a viscoelastic fluid first aligns cells inside a round-shaped capillary (shown in the zoom of Fig. 4) and afterwards guiding them into the entrance of the microfluidic device. Notice that cells are not deformed during their passage of the capillary. Cells enter the microfluidic device vertically from the top and continue proceeding through the different rectangular shaped sections in horizontal directions. We expect

no significant flow disturbances in such a 90° change of flow direction for our microfluidic device.
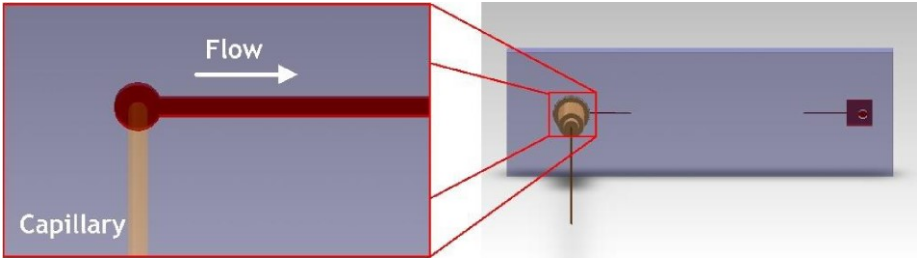

Fig. 4 Zoom section on the inlet region of the microfluidic device.

However, the different consecutive sections of the microfluidic device are schematically represented in Fig.5. In more details, we can see from the image, four different rectangular cross-sections, connected each other by means of hyperbolic contractions. The basic idea is to induce cells movement in a rectangular cross-shaped device with a sequence of sections of different geometrical features, to prevent cells entering immediately into a constrained region and to guarantee unperturbed fluid-flow conditions.
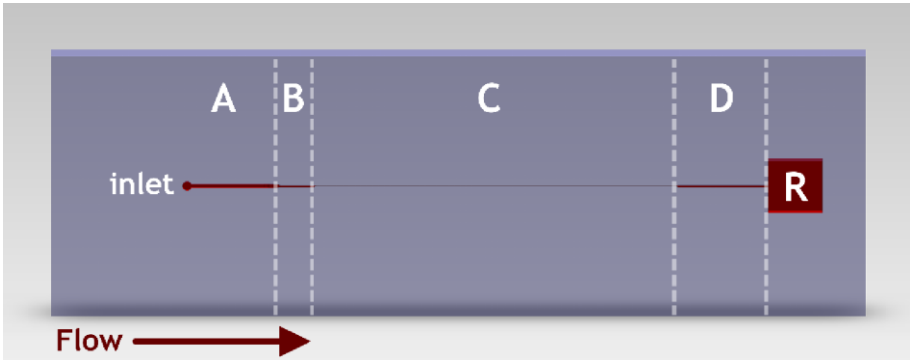

Fig. 5 Schematic representation of the microfluidic device with the four rectangular cross-sections (A-D) and the fluid reservoir (*R*) at the end.

From literature, it is known that hyperbolic connections, calibrated on the differences in channel width (W) of different sections, avoid the formation of upstream vortices or fluid-flow instabilities [48]. Indeed, the design of the contracting regions are based on the computation of a hyperbolic equation, that takes into account the jump from the wider to the narrow channel W. The equation is here reported [49]:

$$w(x) = \frac{1}{\frac{2}{L_C}\left(\frac{1}{W_N} - \frac{1}{W_W}\right)x + \frac{2}{W_W}} \tag{1}$$
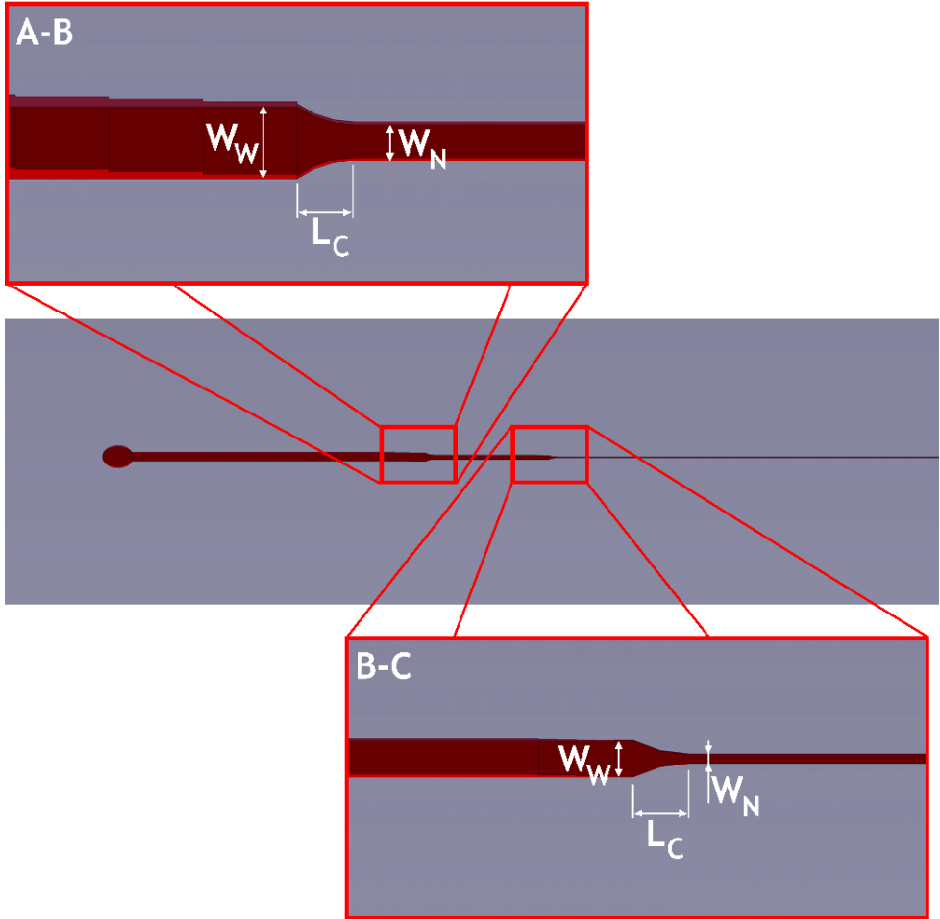

Fig. 6 Zoom-in of the two contraction regions, A-B and B-C in the channel, specified in terms of length of contraction (L_C) and widths of the wider and narrow channels.

Indeed, we expect no fluid viscosity alterations in jumping from one section to another, due to the imposed extensional flow condition. Furthermore, by simulating such a kind of fluid flow contraction behaviour, we verified that the computational flow field in the converging region was not a Poiseuille-like response. After L_C, the channel developed with a length big enough to define a renewed Poiseuille profile. We further characterized the contraction regions by means of a contraction ratio (CR), related to the Hencky strain experienced by the fluid. The parameter is equal to the ratio between the wide and the narrow widths (W_W/W_N) or, equivalently, between the wide and narrow heights (H_W/H_N) [50]. In microfluidic regimes it is possible to guarantee stability conditions to the fluid flow, working at CR values of less than 10 [51]. Particularly, in our case CR was equal to 2 for W and 3 for H at all points of contraction, demonstrating also that no extensional stresses are built and no extensional viscosity variations are recorded [50,51]. Such a kind of CR values enhanced the effect of a hyperbolic contraction, because tuning the viscoelasticity of the medium and the laminar regime, they allowed the reduction of vortex formations going from one section to the other. Indeed, for Newtonian-like behaviours and moderate elasticity of the fluid, we limited the growing process of vortices [51]. For fabrication necessities the hyperbolic contraction has been realized only for the W and not for the H. However, we guaranteed to work in unperturbed fluid-flow conditions and in absence of particle accumulations, designing multiple steps of different H, moving from the wide to the narrow channel (see Fig. 6 for zoom-in images on A-B and C-D contractions). W and H of each section were chosen according to necessities of specific values of aspect ratios ($AR_{Channel}$, given by W/H) and blockage ratios (β, given by d_{Cell}/H, where d_{Cell} is the cell diameter). $AR_{Channel}$ values were fixed in order to fall into workable ranges for a

pressure-driven Poiseuille flow in steady state conditions for infinite parallel plates. No analytical solutions are known for the Poiseuille profile in rectangular cross-sections, but very useful approximate results can be applied in the limit of an almost flat (H<<W) and wide channel. We were conscious that for values $AR_{Channel} \sim 1/3$, the error of approximation could be higher than the one for $AR_{Channel} = 1/10$ [52]. However, our values are exactly in such kind of range and moreover we could expect that in all sections a good Poiseuille profile would be maintained. The βs were chosen in order to avoid a direct contact between cell and channel-walls. Actually, β values influenced also the capability of the cells to stay aligned along the centreline of the channel. By tuning the viscoelastic properties of the fluid, we would expect that, gradually decreasing H and increasing β, the superimposed viscoelastic forces become stronger and vice-versa. In particular, section C is the most important region of our microfluidic device, where we assumed that cells would be able to significantly deform under the viscoelastic action. After C, an expansion ushers in section D. We adapted the hyperbolic function (eq. (1)), used for designing of contraction regions, also for C-D region (see Fig. 7). We chose CR values following the same reasoning applied in the case of converging parts (Table 1).
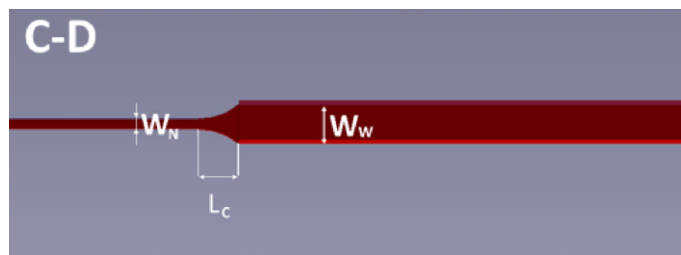

Fig. 7 Illustration of a zoom-in of the expansion region C-D.

We would expect that if D would be long and wide enough, cells could also relax from the constrained condition, travelling toward the reservoir. Furthermore, as we are going to specify in the following sections, C is the section, where deformed cells would be expected.

In the following Table, all of the characteristic dimensions and geometrical parameters of the presented microfluidic concept are reported.

Table 3: Geometrical features of each rectangular sections of the microfluidic concept are shown (height H, width W and length L). We report the $AR_{Channel}$, CR_W and CR_H which stand for contraction ratio of the widths and of the heights, respectively.

Section	H (µm)	W (µm)	L (µm)	$AR_{Channel}$	CR_W	CR_H
Capillary	150*	/	35 (cm)	1	/	/
A	250	400	10000	2	2	3
B	70	200	4000	3	2	3
C	25	100	40000	4	2**	3**
D	90	200	10000	2	/	

*Capillary diameter.
**Expansion data for C-D region.

We fabricated the microfluidic device in poly-methyl-methacrylate (PMMA), by means of a micromilling technique. Micromilling is a fabrication method that creates microscale features using cutting tools that remove the bulk material. A CNC (Computer Numerical Controlled) based micro-milling apparatus (Mini-Mill/GX, MINITECH MACHINERY CORPORATION) was used for device production (see in more details in Fig. 8). Such a micromilling offers two important advantages: the work piece can be milled in few time, minimizing the production step from the design concept to the prototype realization. On the other hand, micromilling fabrication procedure offers the direct possibility to change channel depths creating different steps of height in one device. Indeed, the instrument

consists of a worktable for the X-Y movement, a spindle that keeps in position the cutting tool and allows movement in Z-direction. Of course, the change in height is abrupt but not crucial thanks to the presence of the gradual steps. Such an idea of adding steps for cross-section changes comes from the experimental qualitative observation with other microfluidic devices (in-house production) where flow conditions of particles moving into a fluid remain unperturbed despite the presence of height dimension changes. Then, we felt confident to exclude the presence of possible vortices or turbulences affecting the flow. The entire microfluidic platform was constituted by two pieces of PMMA, the one where the channels were milled and the cover on which we applied a plug connector (NanoPort Assy headless kit (UP N-333), IDEX) for the capillary (Figs. 3-4) and that is used to close the device.
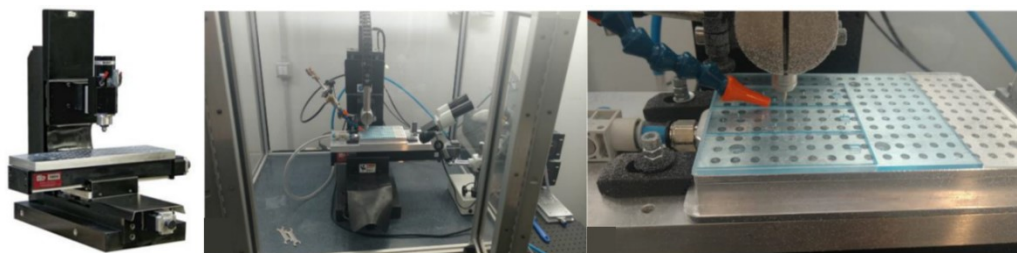

Fig. 8 A 3 axis micromilling is reported. In the middle and on the right, figures show the instrument at work.

After device production and before passing to the bonding phase, we verified the channel depth by means of a profilometer (Veeco Dektak 150, VEECO INSTRUMENTS INC.). It takes surface measurements using contact profilometry techniques at high resolution. All of the channel sections

showed a good match of the measured heights with respect to the designed ones, as we can see from Fig. 9.

For the PMMA bonding (top with bottom), we relied on the use of 10 couples of magnets to create magnetic fields strong enough to close, in a reversible way the microdevice. This simple-to-use connection employs a square-shaped magnet on one side of the microfluidic chip and another one on the other side, providing an interfacial force that keeps the two layers of PMMA together.
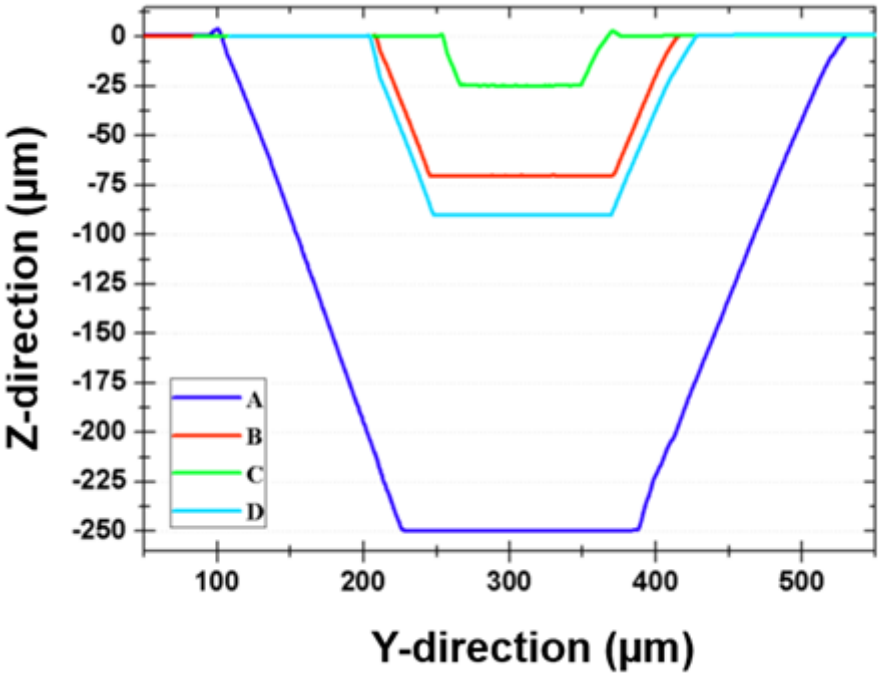

Fig. 9 Profilometer results for each section of the microchannel.

2.2. Fluid-flow concept.

To study alignment and extending beyond deformation of single cells under viscoelastic flow conditions, we use a highly biocompatible polyethylene oxide (PEO, 4Mda, Sigma Aldrich). In order to compute the velocity and stress profiles in our microfluidic chip, we first assume, that the fluid moves between two parallel plates (wide-slit geometry) under a pressure-driven flow. A cartesian reference frame is selected (Fig. 10a), denoting with x the flow direction, y the neutral direction and z the gradient direction, orthogonal to the plates. By assuming incompressibility and neglecting any inertia term of the medium, the governing equations for the problem are:

$$\nabla \cdot \underline{\sigma} = 0 \tag{2}$$

$$\nabla \cdot u = 0 \tag{3}$$

$$\underline{\sigma} = -p\underline{I} + 2\eta_S \underline{D} + \underline{\tau}, \tag{4}$$

defined as the momentum balance, the continuity equation and the fluid stress tensor expression, respectively. Hereby, $\underline{\sigma}^-$, u, p, $\underline{I}$, η_S, $\underline{D}$ are stress tensor, velocity vector, pressure, unity tensor, solvent Newtonian viscosity, and rate-of-deformation tensor, respectively. Moreover, the viscoelastic stress tensor can be specified by the Giesekus equation model:

$$\lambda \underline{\tau}_{(1)} + \underline{\tau} + \frac{\alpha\lambda}{\eta_P} \underline{\tau} \cdot \underline{\tau} = 2\eta_P \underline{D} \tag{5}$$

where λ is the relaxation time of the fluid, η_P is the polymer viscosity and $\underline{\tau}_{(1)}$ is the upper-convected time derivative, expressed as:

$$\underline{\tau}_{(1)} = \frac{D}{Dt}\underline{\tau} - \left\{\underline{\tau} \cdot \nabla u\right\}^T - \left\{\underline{\tau} \cdot \nabla u\right\} \tag{6}$$

The non-dimensional parameter α defines the shear-thinning behaviour of the viscoelastic fluid if greater than 0. When α goes to zero, the fluid has a constant viscosity and the Giesekus constitutive equation degenerates into the Oldroyd-B model [53],

$$\lambda \underline{\tau}_{(1)} + \underline{\tau} = 2\eta_P \underline{D} \tag{7}$$

The overall zero-shear viscosity η_0 for the Oldroyd-B fluid model, as well as for the Giesekus one, is given by the summation of the solvent and the polymer viscosity contributions

$$\eta_0 = \eta_S + \eta_P \tag{8}$$

In this work, we choose to model the viscoelastic medium by the Oldroyd-B constitutive equation, to describe its behaviour. Furthermore, the governing equations can be made dimensionless by imposing the channel height (H) as characteristic length. Thus, the most relevant non-dimensional geometrical channel design parameters are β and the $AR_{Channel}$.

The fluid-flow condition can be modelled by:

$$Re = \frac{\rho \underline{U} D_h}{\eta_0} \tag{9}$$

$$Wi = 2\lambda \overline{U} / H \tag{10}$$

$$El = \frac{Wi}{Re} \tag{11}$$

the Reynolds (Re), Weissenberg (Wi) and Elasticity (El) numbers, respectively. We can further recall ρ as the fluid density, $\overline{U}$ as the average fluid velocity, D_h the characteristic hydraulic diameter of a capillary or duct. In other words, Wi defines the product between characteristic time scale of the fluid flow and time scale of the material fluid, Re relates inertial and

viscous components of the fluid flow condition, while *El*, defines the importance of inertial components with respect to elastic ones.
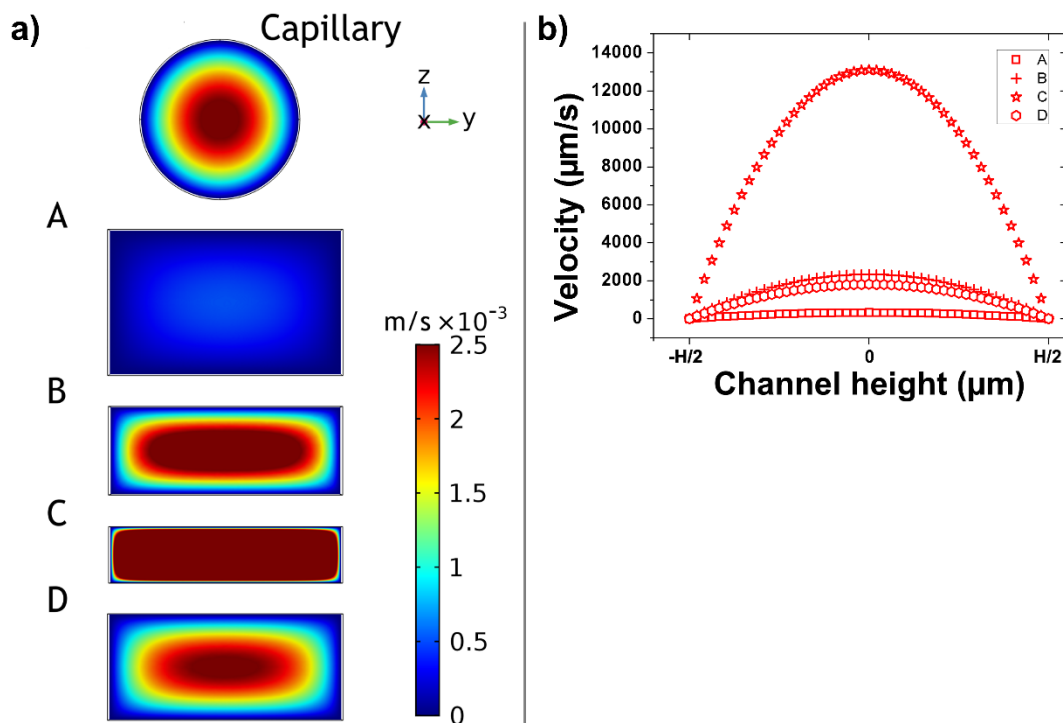

Fig. 10 Velocity profile simulations of the microfluidic chip sections. (a) Representative velocity distribution for all sections of the microfluidic chip and the inlet capillary are reported in sequent fluid flow order from the top to the bottom. All simulations were calculated using a PEO 0.9 and an applied pressure ΔP= 800 mbar and a capillary R=75 μm. All of the sections were simulated using the Multiphysics 5.3a package COMSOL. The velocity scale bar is reported looking at the velocity profile present into section D. This is the reason why the contour plot of section C presents only a very slight variation of the velocity profile with respect to the z-y directions. The velocity appears to be the highest everywhere, since the actual maximum velocity in section C is greater than the one reported in section B. (b) Velocity profile over channel height for each channel section is presented, using a self-written Matlab R2019a routine, showing the parabolic Poiseuille fluid flow condition for all sections.

We investigated η of scaling PEO-concentration (0.1, 0.2, 0.3 until 2.0 wt%), with a stress-controlled rheometer (MCR 302, ANTON PAAR, double cuvette geometry, Fig. 11). We highlighted PEO 0.9 (black), 0.5 (grey) and 0.2 (light grey) concentration used in this work, which correspond to following

polymer concentration 0.88, 0.53 and 0.22 wt%, respectively. They have been further classified as entangled (PEO 0.9), semi-diluted (PEO 0.5) and diluted (PEO 0.2), depending on their own intrinsic viscoelastic properties (Fig. 11a). We applied the Cox-Merz approach (reciprocal of $\dot{\gamma}$ at which storage and loss modulus cross each other the first time) for high polymer concentration to obtain λ values of the liquid (Fig. 11a and d). The median decrease of η values (crossing point versus η_0) indicate when shear thinning behaviour of the liquid gets significant and therefore its λ. For even smaller polymer concentration, where such an approach was inapplicable, a standard Bird-Carreau approach was additionally applied to fit η curves and obtain the searched for λ values. We plotted a master curve which directly related η_0 to λ values (Fig. 11b) and used the following outcome λ = 0.97, 0.38 and 0.11 ms for PEO 0.9, 0.5 and 0.2, respectively for further calculations. In this work, only PEO 09 shows an evident shear thinning behaviour at high shear rates (~ 10^2 s^{-1}, Fig. 11a). However, since the computed maximum velocities for Newtonian and Non-Newtonian Poiseuille flows are similar even in such condition, we have chosen to model all PEO concentrations with the Oldroyd-B constitutive equation, neglecting shear dependence.
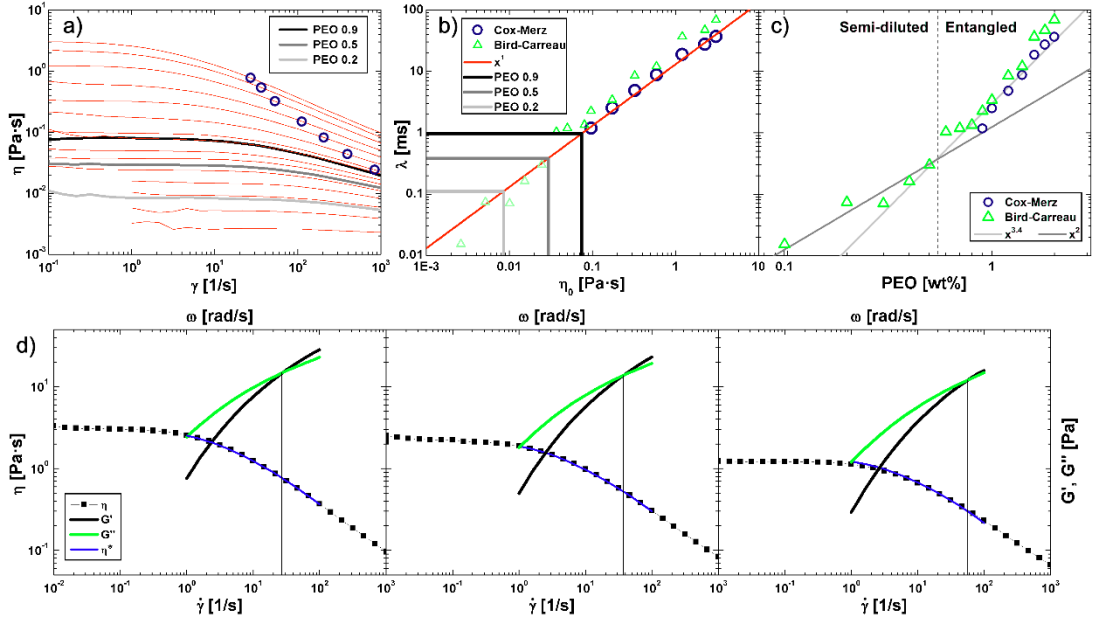
Fig. 11 Rheological fluid investigations. a) Shear-rate-dependent ($\dot{\gamma}$) measurements of the fluid viscosity (η) for a wide range of polyethylene oxide (PEO, 4MDa, Sigma Aldrich) solutions. We highlighted PEO 0.9 (black), 0.5 (grey) and 0.2 (light grey), which correspond to following polymer concentration 0.88, 0.53 and 0.22 wt%, respectively. Green circles indicate the obtained fluid relaxation times (λ) based on the Cox-Merz approach, where shear-thinning behaviour gets significant [53]. In particular, η values (including the complex viscosity η^*) of the crossing point between storage (G') and loss (G'') modulus (shown in d) are related to η_0 values for high PEO concentration (2.0, 1.8 and 1.6 wt%). The hereby calculated median decrease of η value was applied on further PEO concentration (1.4, 1.2, 1.0, 0.9 wt%), where no crossing point between G' and G'' can be obtained by the used standard Rheometer approach, until η values are out of measurement range. Parallel analysis using the Bird-Carreau fitting1 of the obtained η curves indicated similar λ outcome (results shown in b by red triangles). b) λ versus η_0 are plotted for the Cox-Merz and the Bird-Carreau approach, showing similar outcome. The PEO concentrations of interest are highlighted as followed: PEO 0.9 (black), 0.5 (grey) and 0.2 (light grey). A direct relationship between λ versus η_0 was obtained. Therefore, any possible value of η_0 can be related to a λ value. c) The entanglement concentration (c* = 0.56 wt%)2, between semi-dilute unentangled regime and entangled regime is indicated. The change of diluted to semi-diluted regime is expected at a PEO concentration of ~0.2 wt%. d) Flow curve results of η versus γ˙ are plotted for PEO 2.0, 1.8 and 1.6 wt% with overlaid frequency sweep outcome for G', G'' and η^* to obtain the crossing point with η. Out of these measurements λ of the PEO solution is measured. Data was obtained using a stress-controlled rheometer (MCR302, Anton Paar) with cone-plate (diameter of 50mm) geometry. Note that all values of λ represent the rheological properties of the viscoelastic liquid, without the presence of cells or rigid particles.

However, for the Oldroyd-B model, the shear dependence of the total viscosity does not play any role. Further, keeping in mind that Wi has to be around 1, we set all of the fluid flow conditions in order to have *Wi≫Re* and therefore *Re≪1*, avoiding any inertial and vortex contribution to the flow conditions [54]. Moreover, cells are assumed to generate no flow disturbances, which can be confirmed by cell *Re* (*Re_{Cell}=β Re*), defined as a scaling version of the one of the viscoelastic fluid -with remaining *Re≪1* condition- avoiding turbulences and fluid flow alterations [55].

Cell alignment and/or deformation conditions are considerate with the following assumptions. Spherical objects migrate in the direction of minimum shear rates ($\dot{\gamma}$) for a Poiseuille flow. In fact, lateral gradients of normal stresses in the full velocity field are responsible for the migration observed in viscoelastic fluids [54,56-58]. The non-deformed object will follow the fluid velocity along a constant direction (maximum velocity for the Poiseuille flow) minimizing perturbations caused by the object itself [56,57]. The viscoelastic stress and force will assume different profiles depending on the channel geometry (circular or rectangular). In general, for a steady-state Poiseuille flow, we can write a simple force balance in the direction of the shear gradient. Forces are balanced at the equilibrium flow positions of the particle (centre line for a tube and both central axis and corners for a duct) [59,60]. We considerate elastic forces only in gradient direction (z-axis) with H<<W, expressed as:

$$F_E \propto C \left(\frac{d_1}{2}\right)^3 \nabla N_1 \tag{12}$$

being proportional to the gradient of the first positive normal stress difference (N_1), defined as:

$$N_1 = 2\lambda\eta_0\dot{\gamma}^2 \qquad\qquad (13)$$

C is a non-dimensional parameter, defined with respect to the chosen fluid [53].

For negligible inertia, F_E can be balanced with Stokes drag (F_D) expressed as:

$$F_D = 6\pi\eta d_1 U_{migr} \qquad\qquad (14)$$

with the migration velocity U_{migr}. Finally, viscoelastic cell alignment can be achieved, if the following relationships is satisfied:

$$\Theta = A_P Wi\beta^2 \frac{L}{H} > -ln\,(3.5\beta) \qquad\qquad (15)$$

with A_P a channel geometry constant and L the minimum length needed to observe a stable centre-line alignment [56, 59]. We specified A_P analytically, starting from the Poiseuille profile for the circular and rectangular geometries, resulting in A_P=3 and 1.5 for capillary and duct shape, respectively.

We used the CFD package of COMSOL Multiphysics 5.3a and Matlab R2019a, respectively for numerical simulations and analytical calculations. The simulations are carried out on physics-controlled meshes of an extra fine element size. The fully developed velocity profile and the shear rate are evaluated by 3D finite element simulations using COMSOL (Fig. 10a and b). From that, we computed the relative intensity of the F_E by calculating $\nabla\dot{\gamma}^2$ that correspondently defines ∇N_1.

2.3. Cell sample preparation.

We have investigated MCF-10A, MCF-7 and MDA-MB-231 cells. MCF-10A were donated from S. Piccolo (Istituto FIRC di oncologia

molecolare, IFOM, Milan, Italy) and cultured in mammary epithelial basal medium (MEBM) supplemented with the mammary epithelial growth media (MEGM) bullet kit (Lonza). MCF-7 and MDA-MB-231 cell lines were kindly donated by Daidone's group and Dr P.F. Cammarata (Institute of Molecular Bioimaging and Physiology, IBFM-CNR, Cefalù (PA), Italy), respectively. MFC-7 cells are cultured in eagle's minimum essential medium (EMEM, Sigma-Aldrich) containing 10% fetal bovine serum (FBS), 100 µg/ml l-glutamine and 100 U/ml penicillin/streptomycin. MDA-MB-231 cells are cultured in a 1:1 mixture of Dulbecco's modified essential medium (DMEM, Euroclone) and Ham's F-12 medium (Microtech) supplemented with 10% FBS, 1% non-essential amino acid mixture and 100 U/ml penicillin/streptomycin. Finally, each investigated cell type is diluted in 500 µl of viscoelastic medium to reach a final cell concentration of circa 50 cells per µl. Furthermore, cells have been checked for Mycoplasma infection using Hoechst 33342 (Life Technologies) DNA staining. We did not observe the presence of stained dots outside the nuclei by using an inverted microscope (X81, Olympus) equipped with a water immersion objective (60x objective with NA 1.35), showing no evidence of Mycoplasma infection.

Cells subjected to different viscoelastic forces are recovered after flux -10 min after measurement start- from the chip reservoir and seeded into separate wells of a µ-Slide (Ibidi). First, cells adhere slightly onto glass surfaces for 10 min, in order to prevent a drastic change of the cell morphology.

For immunostaining, cells were fixed with 4% paraformaldehyde (Sigma-Aldrich) for 15 min at room temperature, then rinsed twice with PBS. Permeabilization -with 0.1% Tryton X-100 (Sigma-Aldrich) for 5 min- was performed only for Actin Cortex, Microtubule Network, Lamin A/C, YAP

and cGAS investigation. Thus, Actin Cortex was stained at the level of F-Actin components with Alexa 488 phalloidin (Invitrogen) at 1:200 dilution for 1 h. Microtubule Network, instead, was stained with Beta III Tubulin monoclonal antibody overnight at 4°C with Alexa543 anti-mouse secondary antibody. At the nucleus level, Lamin A/C was stained with monoclonal Lamin A/C mouse antibody (SC-376248) overnight at 4°C and with Alexa488 goat anti-mouse secondary antibody. To analyze the Nuc/Cyt ratio of YAP, cells were incubated with primary YAP1 polyclonal rabbit antibody (PA1-46189, ThermoFisher Scientific) overnight at 4°C and with Alexa543 goat anti-rabbit secondary antibody. Nuclei were counterstained with TO-PRO-3 stain (T3605, ThermoFisher Scientific) at room temperature for 30 min. cGAS staining was performed with primary cGAS rabbit polyclonal antibody (HPA031700 Sigma-Aldrich) overnight at 4°C. cGAS antibody was donated from T. Panciera (University of Padova, Padova, Italy). Finally, cells were washed with PBS for three more times. To monitor the Hoechst entry into the nucleus, on not yet stained samples, we added a solution diluted at 1:1000 of concentration, by recording the molecule entry in 600s of measurement. Chromatin images have been collected at the end of the transitory time of Hoechst entry, so that waiting 30 min as usual time for staining procedures. For the highest viscoelastic solution concentration, also a standard 'Trypan blue test' was performed, to monitor the cell viability over time. In particular, despite of the absence of a functional vitality response in MDA-MB-231, we observe that a 100% of cell viability was guaranteed.

2.4. Experimental procedure and Data Analysis.

2.4.1. In-flow deformed cells dynamics.

We defined different experimental measurement positions as followed: Q – quiescent measurement (off-chip), T_B – in-flow measurement in the beginning of B (on-chip) and T_D – in-flow measurement in the beginning of D (on-chip). T_E – quiescent measurements of living cells directly after in-flow cell deformation (off-chip). Firstly, we performed off-chip investigations (Q) of biophysical un-deformed cell parameters using a confocal laser scanning microscope (LSM 710, Zeiss) equipped with argon and He−Ne laser lines at the wavelengths of 488 and 543 nm, respectively. Secondly, we performed in-flow cell investigations (T_B and T_D). Hereby, before each measurement, capillary tubing and microfluidic chip are flushed with ethanol-H2O mixture of 50% for 10 minutes and subsequent with PBS solution for 15 minutes. In addition, for each in-flow investigated cell class a new capillary tubing is used. A three-fold higher flow rate compared to measurement condition is used to fill the microfluidic system with the viscoelastic medium. Afterwards the cell sample is placed in the pressure pump and pushed with the measurement flow rate through the microfluidic chip. Measurements are initiated 5 min after filling procedure start to allow the chip to equilibrate. In a typical experiment duration of 20 seconds circa 0.74 µl of cell suspension is pushed through the chip and investigated by the imaging system (~50 cell/µl). Such performance result in a total amount of around 35 cells per measurement, ensuring a cell to cell distance of more than 200 µm in C. Of note, experiment duration was limited to ensure constant acquisition rate of 1000 frames per second. Investigated cells are collected in the chip reservoir after 20 min of measurement time (~40 µl of sample

volume) for further off-chip investigations (T_E) using a confocal microscope. Cells which pass the chip during the filling process are discarded. However, to enable a versatile tracing of morphometric and dynamic cell details in flow condition, we use a 10x objective and a field of view of 2048x200 squared pixels (0.65 µm/px), which covers a final cell tracing length of 1.33 mm (t_1 to t_2) in the beginning of D. Of note -for all experiments- we performed cell investigations with constant cell velocities in C. Such flow requirement implies a change of the capillary dimension and applied pressure to achieve sufficient cell alignment in all sections of the microfluidic chip (Fig. 13).
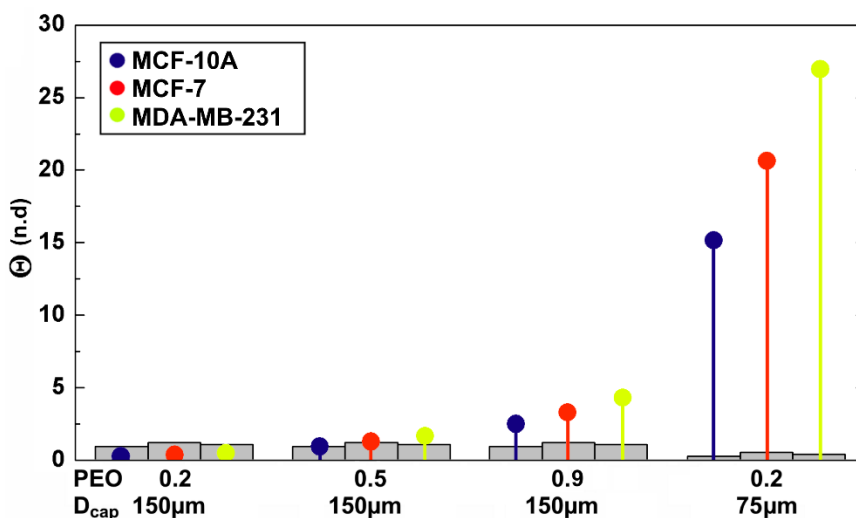

Fig. 13 Cell alignment probability (Θ) for viscoelastic liquid and cell classes. The grey bars indicate the threshold ($-ln$ (3.5β) to ensure cell alignment. In cases of insufficient cell alignment, the capillary diameter (D_{cap}) was reduced from 150 to 75 µm (last case on the right).

Third, we performed off-chip investigations at T_E, analysing biophysical cell parameters using the already mentioned confocal microscope.

In-flow cell analysis are performed at T_B and T_D and are divided into two main steps. First the dynamic cell motion parameters are investigated over

the full cell tracing region. Second the average cell deformation parameters of interest are extracted for each investigated cell line for classification.

The former analysis approach implies the measurement of several dynamic in-flow cell parameters, such as major axis (d_{Cell}), minor axis (d_2), area (A), perimeter (P) and orientation angles (φ_i), at the beginning (t_1) and end (t_2) of the cell tracing region (Fig. 15a and 16a and b). Out of such parameters cell aspect ratio (AR) and cell deformation (CD) are calculated as followed:

$$AR = \frac{d_{Cell}}{d_2} \qquad (18)$$

$$CD = 1 - c = 1 - \frac{4\pi A}{P^2}, \qquad (19)$$

where c is the object circularity [25].

In the specific case of rolling motion of cells, we computed the variation of the cell orientation angle as follows [61]:

$$T_{rev} = 2\pi(AR + AR^{-1})\dot{\gamma}^{-1} \qquad (20)$$

$$\tan\varphi = AR\tan\left(\frac{2\pi t}{T_{rev}}\right) \qquad (21)$$

In addition to the previously mentioned in-flow cell analysis, we measured such cell parameters before (Q - Table 3) and at T_E using a confocal microscope.

Table 3 Mean values and standard errors of the measured AR and CD observed at confocal microscope before flux (n=30, 30 and 30 for MCF-10A, MCF-7 and MDA-MB-231, respectively).

Cell Type	AR (a. u.)	CD (a. u.)
MCF-10A	1.054 ± 0.005	0.021 ± 0.001
MCF-7	1.049 ± 0.005	0.017 ± 0.001
MDA-MB-231	1.076 ± 0.008	0.018 ± 0.001

All results are presented as the mean $\pm$ standard error. When normality assumptions were met, the statistical significance for two or more groups of data were calculated by using a one-way ANOVA with corresponding Tukey's multiple comparison. When normality assumptions were not met, nonparametric statistical tests (pairwise Wilcoxon–Mann–Whitney test) were performed. Significance are indicated by p values (nsp > 0.05; *p < 0.05, **p < 0.01, ***p < 0.001) combined with F-values. We used Excel 2016 (Microsoft Corporation) for all statistical analyses.

To measure possible object blurring effects in-flow, PSL are investigated in B at different velocities using the camera frame rate of cell measurements. The measurement duration is limited to 20 seconds and repeated three times. Out of such investigations, an average particle CD_{PSL} versus particle velocity can be obtained (Fig. 14). We measured incorrect particle deformation ($CD_{PSL} > 0.01$) for velocities above 2600 $\mu m\ s^{-1}$. So, we limited experimental measurements to a maximum cell velocity of 2100 $\mu m\ s^{-1}$ avoiding possible blurring effects from the imaging system recordings. Moreover, we tested our measurement approach by evaluating the aspect ratio of PSL (AR_{PSL}) in D at the maximum PEO concentration condition and at the velocity applied during the cell experiments, verifying an absence of a significant particle deformation ($AR_{PSL} = 1.083 \pm 0.004$, with $n = 31$).
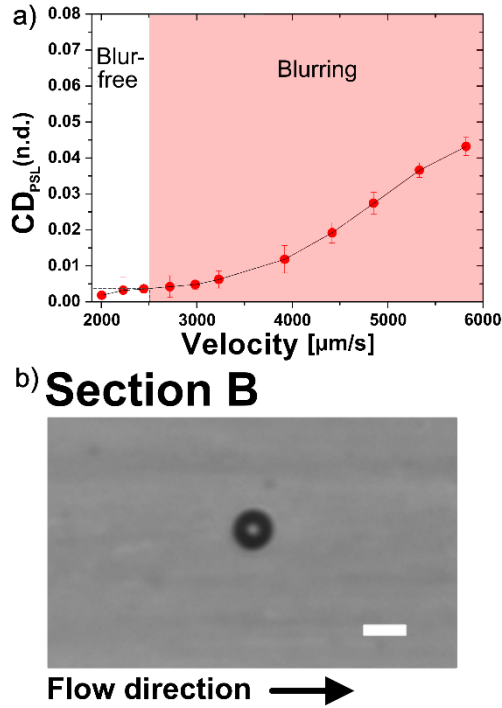
Fig. 14 PSL beads measurements at different fluid velocities. a) Cell deformation versus particle velocity is plotted. The highlighted red area indicates CD values, for PSL particles, above 0.01, which are considerate as blurring (n>10 for each data point). Therefore, cell measurements should be performed below 2500 µm s-1 for the used camera settings (1000 fps, ET<5 ms). Error bars are presented as standard deviation of the mean. b) An image of a polystyrene bead without blurring effect is presented.

2.4.2. Lamin A/C, YAP and Chromatin condensation analysis.

We defined different off-chip measurement steps as Control and PEO 05 or PEO 09 to be the quiescent measurements of stained cells before and after in-flow compression at the two PEO conditions. Actually, we decided to test cells in Control condition both with PEO 05 and 09 in order to appreciate possible differences in the not-deformed configuration depending on the chosen PEO solution. In order to do this, we added PEO 05 and PEO 09 diluting them with the medium where cells have been treated.

Then, we tested alive cells in-flow by inducing deformation at both PEO 05 and PEO 09, fixing and staining cells after these two compressive forces. Firstly, we performed Lamin A/C and nucleus investigations at Control, PEO 05 and PEO 09 conditions using a confocal microscope (TCS STED CW, LEICA) in a modality resonant scanner (8Hz), equipped with a 100× oil-immersion objective (NA 1.4). Secondly, observing the Lamin A/C modification, we acquired images coupling YAP and Lamin A/C signals, again by using STED confocal microscope. Image resolution was fixed at 1024×1024 squared pixels with a 2× zoom factor. In addition, we collected three dimensional representations of cells at Control, PEO 05 and PEO 09 conditions in MCF-10A and MDA-MB-231 as representative cases of the obtained results. Image stacks, covering the total cell volume, were collected at 0.27 μm Z-spacing using a 63× oil immersion objective (NA 1.4) of a confocal laser scanning microscope (LSM 710, Zeiss) equipped with an argon and HeNe laser lines at the wavelengths of 488 and 543 nm, respectively. Image resolution was fixed at 512×512 squared pixels with a 4× zoom factor. Except for image stack acquisition, also cGAS-Lamin A/C images were collected with the LSM confocal laser microscope, with the same acquisition specifications. Hoechst entry and chromatin images were saved by using Olympus Cell-R equipped with a 60× water-immersion objective (NA 1.3). Image analysis has been carried out with ImageJ and Fiji software. For the Lamin A/C level quantification, we normalized the value of the single-channel intensity with respect to the area delimited by the Lamin A/C itself. Then, we defined the Lamin A/C coverage as the portion of the nuclear perimeter occupied by the Lamin A/C with respect to the entire available nuclear perimeter. We performed such a kind of analysis, by using the 'Analyse particles' Fiji plugin on images with applied threshold, in order to

detect the Lamin A/C constituent parts and then summing the single particle perimeter to get the total Lamin A/C perimeter. We applied the same threshold value as well as Gaussian filtering definition for the images in order to make them in proper comparison. YAP signal has been estimated by computing the ratio between the normalized integrated densities of the nucleus and of the cytoplasm, before detecting the respective nucleus and cell areas. For cGAS analysis, the single-channel intensity values have been collected after a Gaussian filter of the image and correlated to the respective Lamin A/C. Hoechst intensity has been measured by collecting the value of the nucleus area normalizing the intensity values on it. This procedure for each instant of time reveals how the signal changes during the time. To quantify the level of chromatin condensation, we processed fluorescence microscope images by using an edge detection algorithm. In more detail, the condensation of chromatin increases the number of distinct spaces within the nucleus, which can be detected by a Sobel edge detection algorithm (pixel reduction factor = 2 and Sobel threshold = 0.02). Thus, measuring the density of edges within the nucleus, normalized to its cross-section area, gives a measure of the level of chromatin condensation defined as CCP [62].

For simplicity, we adapted with correction factors -with respect to Control PEO 05- all of the measured parameters of the after flow PEO 09 condition, in order to simplify to read the final results. Being conscious that a statistical comparison of the resulting data, with the correction factors, is not possible, we reported original raw data into box chart plots correlating them with the respective error bars defined by the application of a Kruskal-Wallis statistical test.

2.4.3. Actin Cortex and Microtubules investigation.

We defined different off-chip measurement steps as Control (CTRL) and PEO 09 to be the quiescent measurements of stained cells before and after in-flow compression. In order to have comparable results, we added PEO 09 to CTRL diluting it until a PEO 05 concentration. Then, we tested alive cells in-flow by inducing deformation at PEO 09, fixing and staining cells after these two compressive forces.

Additionally, target-specific drugs are employed to induce cytoskeletal perturbations. We decided to test CYTD from Sigma-Aldrich at 37 °C for 30 minutes, at a final concentration of 30 µM in serum free medium to inhibit actin polymerization and disrupt main actin filaments. For microtubules, cells were treated with NOCO to destabilize microtubules, which consequently promotes their depolymerization. NOCO (Sigma-Aldrich, M1404) was dissolved in 1ml of dimethyl sulfoxide and 100 µg of the dissolved drug was further dissolve in 5ml of culture medium. From this, the necessary volume was added to the cells while adherent to obtain the needed concentrations. The treatment duration was of 30 minutes.

Firstly, we performed actin cortex and microtubule network investigations at Control and PEO 09 conditions using a 63× oil immersion objective (NA 1.4) of a confocal laser scanning microscope (LSM 710, Zeiss) equipped with an argon and HeNe laser lines at the wavelengths of 488 and 543 nm, respectively. Image resolution was fixed at 512×512 squared pixels with a 4× zoom factor. Image analysis has been carried out with ImageJ software. For the actin cortex level (Actin Cortex Density) quantification, we normalized the value of the single-channel intensity with respect to the area delimited by the external ring of the cortex itself subtracting it with the

nucleus area. Then, we defined the cortex fragments position and area by using the 'Analyse particles' ImageJ plugin on images with applied threshold, in order to detect the actin constituent parts. We applied the same threshold value definition for the images of the single cell line in order to make them in proper comparison between PEO conditions. Then, the identified fragments are specified in terms of area and centroid position in order to establish the reciprocal distance between the entire cell centroid and the fragment centroid itself. A histogram analysis of such fragments position is proposed, combining to each resulting bin the summation of the constituent fragments areas to appreciate where the bigger fragments are localized. Microtubule signal (Microtubule Network Density) has been computed normalizing the value of the single-channel intensity with respect to the area delimited by the external ring of the cortex itself subtracting it with the nucleus area (Appendix B).

All results are presented with nonparametric statistical tests (Kruskal-Wallis test). Significance are indicated by p values (ns > 0.05; *p < 0.05, **p < 0.01, ***p < 0.001). We used Excel 2019 (Microsoft Corporation) for all statistical analyses.

2.4.4 Intracellular delivery experiments.

We defined two different off-chip measurement steps as Control (CTRL) and PEO 09 to be the quiescent measurements of stained cells before and after in-flow compression. Actually, we decided to test cells CTRL condition adding PEO 09 diluting it until a PEO 05 concentration. In order to do this, we added PEO 05 and PEO 09 diluting them with the medium where cells have been treated. Then, we tested alive MCF-7 cells in-flow by inducing deformation at PEO 09. We seeded cells in the two aforementioned

conditions on Ibidi μ-slide 8 well (Ibidi GmbH, Germany) plates and allowed to adhere for 10 minutes, as indicated in section (2.3). After adhesion, cells were incubated for 20 minutes, at 4°C, with 540 μl of carboxyl-modified fluorescent polystyrene particles (0.2 μm-diameter, Cat. No. 09834-10, and 1 μm- diameter, Cat. No. 15702, Polysciences) at the final concentration of 0.03% v/v in complete growth medium. After incubation, cells were rinsed five times with PBS to remove non internalized microparticles and fixed with 4% paraformaldehyde for 20 min.

We measured the NPs amount by deriving the signal intensity associated to each constituent slice of cells, imaged with a z-stack (slice thickness 0.37 μm) using a 63× oil immersion objective (NA 1.4) of a confocal laser scanning microscope (LSM 710, Zeiss). Then, we normalized such intensity value with respect to the volume of interest calculated as difference between the entire cell and the two excluded parts, on the top and on the bottom of the cell, because of possible signal disturbances. The excluded parts as spherical caps have been chosen computing the 10% of the major radius of the cell (from Analyse-Measurement-Major). For counting, from the selected volumes, we applied a threshold (120 as minimum, chosen from the intensity of one pixel) to detect single particles or aggregates and to measure the volume that they occupy (Voxel Counter Plugin). Thus, we computed the number of objects dividing the occupied volume of the NPs with respect to the volume of a single NP. For 1 μm case, no threshold has been applied since the instrument resolution allows us to clearly distinguish the single object of interest.

All results are presented with nonparametric statistical tests (Kruskal-Wallis test). Significance are indicated by p values (ns > 0.05; *p < 0.05,

**p < 0.01, ***p < 0.001). We used Excel 2019 (Microsoft Corporation) for all statistical analyses.

3. Results and Discussion

3.1. Force computation and calibration.

We estimated the viscoelastic compression forces (F_{EMax}) for different polymer concentration (PEO 0.2, 0.5 and 0.9), by simulating and validating the velocity and shear rate profiles (Fig. 12a and c). A viscoelastic pressure-driven flow is reported by modelling the fluid as an Oldroyd-B. Under these fluid-flow conditions, suspended cells experience F_E emerging from the unbalance of the positive N_1, leading to the alignment of cells moving towards their own equilibrium position at the channel centre line. In our case, the alignment condition is already reached and kept stable inside the round capillary, and then all along the microfluidic chip, allowing cells to perceive the compressive forces always in a symmetric way (Fig. 12b). Moreover, the unperturbed alignment condition leads all cells to stay always at the centre line of the channel section even after deformation, along the expansion region from C to D, thanks to the coupled action of walls confinement and viscoelastic fluid properties. The acting forces are a function of the gradient of the square of $\dot{\gamma}$ and β. We properly calibrated the initial pressure and velocity conditions, as well as the channel geometry, in order to align cells and beyond that to reach higher values of F_E to deform cells in a contactless way. In order to estimate applied F_E and then to choose the desired range in which deformation occurs, we computed F_{EMax} values coming from the channel walls, supposing the cell already at its own equilibrium position where the competing F_E and F_D, are balanced. The reference system coordinates is placed at the centre of the channel section,
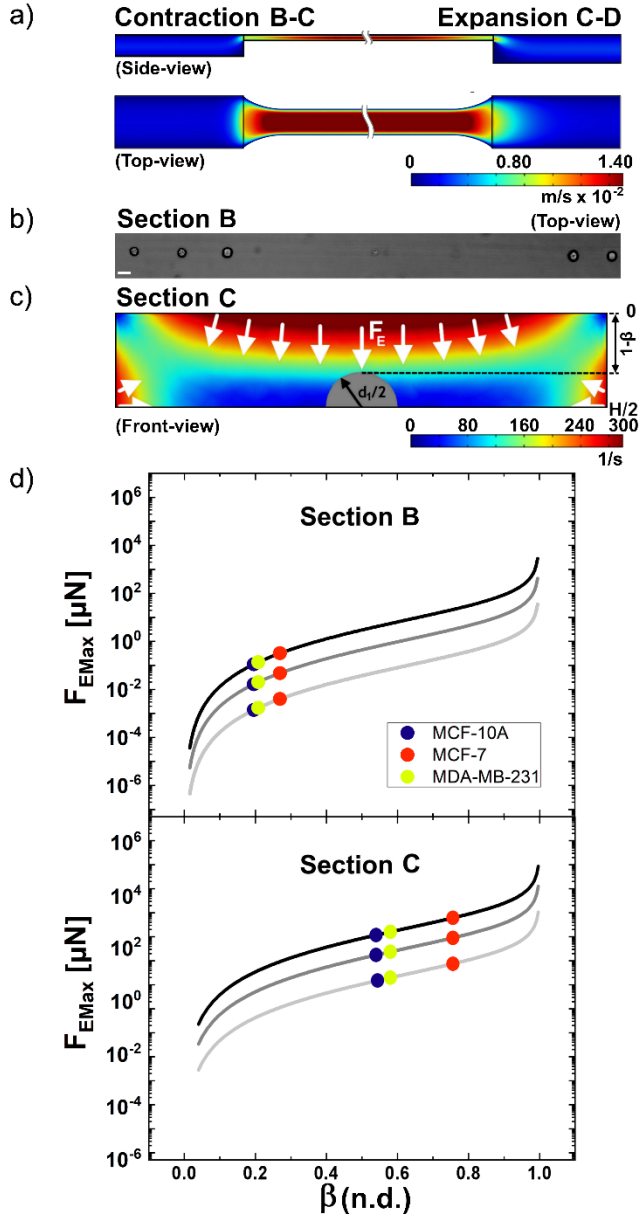
Fig 12 F_E distribution and computation in the microfluidic chip. a) The velocity distribution of the contraction and expansion regions of C, are designed for optimal laminar flow condition and for F_{EMax} condition in C. b) A typical image of 3D-aligned cells in B before in-flow induced deformation in C is shown. Length of the scale bar is 20µm. c) F_E are applied in C as indicated in the representative sketch, which shows the applied shear-rate distribution. d) Computed F_{EMax} in B (top) and C (bottom) with respect to β are shown. Viscoelastic mediums are plotted for PEO 0.2, 0.5 and 0.9 in light grey, grey and black, respectively. Dots indicate β-values for d_{Cell} value before flux.

where the cell centre position is expected. It is assumed that the F_{EMax} scales with respect to the cell dimension by a factor $(H/2 - d_{Cell} / 2)$ that takes into account the variation of the region of channel height occupied by the major cell diameter itself (Fig. 12c).

We found a linear inverse relationship between the force and a "gap-size" due to the presence of the cell itself (Fig. 12c) [63]. F_E is generally defined as [60],

$$F_E \propto C \left(\frac{d_1}{2}\right)^3 \nabla N_1 \tag{16}$$

From the wall, when forces are balanced, we propose the following final analytical expression, for spherical objects:

$$F_{EMax} = -C d_1{}^3 2\eta_0 \lambda \nabla \dot{\gamma}^2|_{z=\frac{H}{2}} \tag{17}$$

$$= 128 U_{Max}^2 \eta_0 \lambda \beta^3 (16\pi(1-\beta)^{-1})$$

where $1 - \beta$ is the "gap-size" due to the cell presence and written as a function of the cell blockage ratio, U_{Max} is the maximum velocity at the channel centre line, η_0 and λ are viscosity and relaxation time of the viscoelastic fluid, respectively. The constant C is chosen to be 16π accordingly to the Oldroyd-B fluid model used in the work [53].

To estimate the possible range of F_{EMax} entities with respect to β -in B and C- we used eq. 17 and we varied d_{Cell}, measured before flux (Table 2 and Fig. 13).

Table 2 Mean values and standard errors of the measured major diameters of cells (d_{Cell}) observed at confocal microscope before flux (n=30, 30 and 30 for MCF-10A, MCF-7 and MDA-MB-231, respectively).

Cell Type	d_{Cell}[μm]
MCF-10A	13.634 ± 0.168
MCF-7	18.959 ± 0.289
MDA-MB-231	14.798 ± 0.240

The observed cell lines are not extremely heterogeneous (Fig. 13), which helps us to be confident in using a mean value of d_{Cell} for the evaluation of F_{EMax}. We reported values of force for each used PEO concentration (Fig. 12d). Moreover, in B and D, we verified a good matching of computed and experimental fluid velocities (~2600 μms^{-1} in B and ~2000 μms^{-1} in D measured with latex particles (PSL) of 8.02 ± 0.10 μm nominal diameter (Sigma Aldrich) , Fig.12a). Such results suggest that the expected values of acting compressive forces are actually those computed with eq. 17. In C, we evaluated a range of F_{EMax} going from 1 μN up to 10^3 μN for increasing polymer concentration.
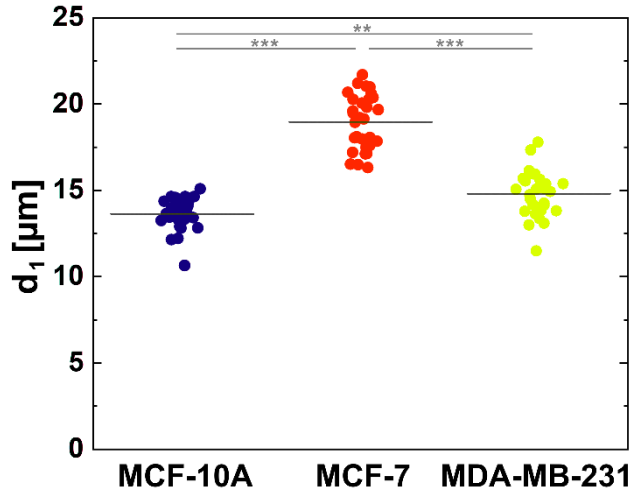
Fig. 13 Values of cell diameters (d_{cell}) observed at confocal microscope before flux. Diameters are plotted for each single cell line (n= 30, 30 and 30 for MCF-10A, MCF-7 and MDA-MB-231, respectively). The mean value of each distribution is indicated by a grey horizontal line. Statistical significances were determined by one-way ANOVA and Tukey's test ($^{ns}p > 0.05$; $*p < 0.05$; $**p < 0.01$; $***p < 0.001$).

Of note, the applied fluid-dynamic condition is the same for all of the applied forces, since the velocity has been fixed for each PEO concentration. So that, FEMax varies only with respect to the cell size, through the third power of β, by minimizing effects possibly due to different fluid velocity conditions, and making easier a comparison between the different cell lines. In fact, we found that MCF-7 perceive a higher force than MCF-10A and MDA-MB-231, that conversely undergo the same compression force having a similar cell size (Fig. 12d).

3.2. In-flow deformation dependent dynamics.

We present a new microfluidic approach to apply, over a wide range, tuneable compressive forces on suspended cells, which result in well distinct

signatures of deformation-dependent dynamic motions. By properly conceiving microfluidic chip geometry and rheological fluid properties, we modulate applied single-cell forces, which result in different motion regimes (rolling, tumbling or tank-treating) depending on the cell line. We demonstrate a breast cancer cell classification from a set of in-flow parameters (orientation angle, aspect ratio, cell deformation and cell diameter) as a backward analysis of cell mechanical response. By such approach, we report that the highly invasive tumour cells (MDA-MB-231) are much more deformable (6-times higher) than healthy (MCF-10A) and low invasive ones (MCF-7).

3.2.1. Cell deformation measurements.

We performed a full on-chip characterization showing cell parameter outcome based on AR and CD (Fig. 15b). Of note, both mean values of AR and CD at T_B perfectly match the off-chip data before flow at Q (Fig. 15b and Table 3). At T_B, at the highest PEO concentration, we confirmed the absence of cell deformation with all the cell lines starting from a similar mean AR and CD value (Fig. 15b). Instead, at T_D, we monitored cell deformation at two measurement positions fixed immediately after compression releasing, where the expansion region ends (t_1 - light grey highlighted part in Fig. 15a). and at the end of the region of interest (t_2 - Fig. 15a) established by the observation area (1130x130 µm in D) of the imaging system. Cells, coming from C, go through the expansion region flowing at the channel centre line, keeping stable the equilibrium position and then starting from the same initial position once they arrive in D. AR and CD variation makes evident the differences in the non-linear mechanical properties among the cell lines. In fact, CD increases for MCF-10A, from the lowest to the intermediate F_E,

while it slightly increases at the highest PEO concentration. AR also changes in a similar trend, sensibly increasing from PEO 05 to 09 (Fig. 15b - light grey highlighted part). MCF-7 express analogous variations, both for AR and CD, almost reducing the mean deformation degree at the highest F_E. Such mechanical responses suggest that MCF-10A and MCF-7 strengthen upon high levels of imposed force and at large deformation. Completely different is the case of MDA-MB-231. The mean AR increases by 2.4-fold with respect to Q condition, while MCF-7 changes by 1.85-fold despite perceiving a higher F_E. However, major CD differences among the cell lines are attested for the intermediate and the highest F_E (Fig. 15b - light grey highlighted part). Indeed, at highest applied F_E, MCF-10A and MCF-7 reach mean CD values of about 0.160 compared to MDA-MB-231 with 0.280. It is clear that MDA-MB-231 tend to soften once subjected to high levels of compression. This is in good agreement with experimental data that demonstrate highly invasive tumour cells to be softer than healthy and low metastatic cell lines, that appear to be more rigid [7]. Such evidences raise speculation that cancer cells might adaptively soften to facilitate migration and invasion of narrow tissue spaces [7, 64]. So that, the proposed microfluidic approach enables, for each cell line, a simple compression test at a certain level of force, then allowing a deep study of the cell specific mechanical response.
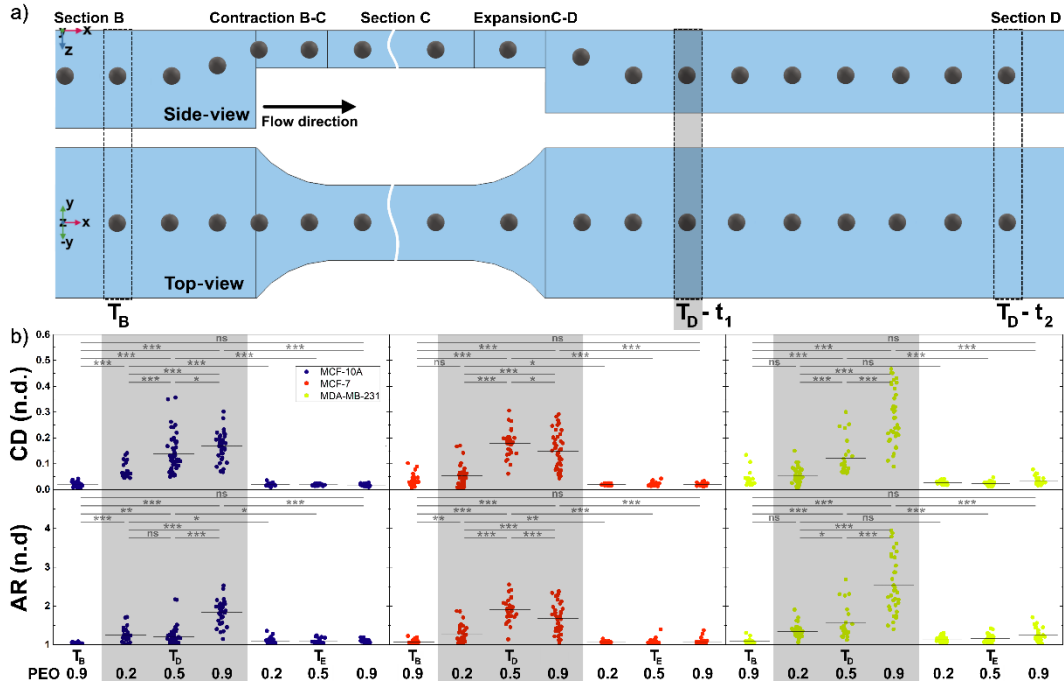
Fig. 15 *AR* versus *CD*. a) Sketch of the microfluidic chip indicate the measurement positions for cell parameters. Time points t_1 (start) and t_2 (end) -of the observation area in D- indicate the measurement positions for the in-flow deformation-dependent dynamics of cells. b) Cell parameters outcome of *AR* and *CD* are plotted for each single cell line from lowest to highest applied F_E (MCF-10A: n=31, 25, 51, 35, 30, 30 and 27; MCF-7: n=29, 33, 28, 42, 30, 30 and 30; MDA-MB-231: n= 19, 35, 26, 35, 27, 30 and 29 for T_B - PEO 0.9; T_D - PEO 0.2, 0.5, 0.9; T_E - PEO 0.2, 0.5 and 0.9, respectively). T_D values are represented for t_1 condition and highlighted with light grey background. The mean value of each distribution is indicated by a grey horizontal line. Statistical significances were determined by one-way ANOVA and Tukey's test (^{ns}p > 0.05; *p < 0.05; **p < 0.01; ***p < 0.001).

3.2.2. In-flow dynamics of deformed cells.

Simultaneously to *AR* and *CD* evaluation, we performed measurement and detection of in-flow motions of the deformed cells, to classify them. Then, we already conceived the asymmetric cross-section change from C to D to impose different in-flow deformation-dependent motions, starting from equal flow conditions as well as initial position, same cell trajectories and

viscoelastic fluid properties, for all cell lines. The analysis were performed in top-view in T_D (Fig. 16a), identifying three possible motion regimes as rolling (R), tumbling (T) or tank-treading (TT) [26]. We measured cell orientation angle (φ), seen as the object inclination with respect to the flux direction (Fig. 16b) [28,65]. In general, deformed cells behave as oblate spheroids, rotating around their minimum axis [26]. We adopted the reference system of the force computation assuming that cells behave like rigid bodies, since D has been conceived to avoid any further deformation (Fig. 16b). We observed that when the major axis is in the yx-plane, the cell simply tumbles. Highly deformed cells do not change their mean orientation, but they minimally oscillate around that, describing a TT motion. Instead, cells with a low degree of deformation move as R motion (Fig. 16a and c). As long as the cell does not fully R or TT in the yx-plane, the temporal evolution of φ could be described by a period of revolution (T_{rev}) as a function of $\dot{\gamma}$ and AR, using eq. 20. We computed the φ evolution with the orbit equations derived from Jeffery implanting eq. 21 and fitting the experimental values of φ with the temporal equation, obtaining satisfying results for MCF-7 (Fig. 16c). We demonstrate that the cell motion strictly depends on the entity of deformation (Fig. 16c and e). The general angle θ_i is an orbit angle, measurable in side-view and directly related to φ_i through the already mentioned Jeffery orbits results [66]. Since our observations are performed in top-view, we evaluated φ_i, in the range of $[-90°: 90°]$, reporting such values at t_1 and t_2 (Fig. 15a and 16a). At t_2, we showed the change of inclination in T motion, specifying how the rotation occurs.

Then, we computed an angle variation ($\Delta\varphi$) taking φ_1 and φ_2 at t_1 and t_2, respectively. We plotted $|\Delta\varphi| = |\varphi_2 - \varphi_1|$ versus CD for each cell class and PEO to retrieve the different cell movements in-flow (Fig. 16e). For low

entities of F_{EMax}, CD remains low with corresponding low $\Delta\varphi$ values, as generally present in the case of R ($CD\sim$ (0; 0.15) and $\Delta\varphi \sim 0°$). For increasing F_{EMax}, cells show a narrow range of CD at higher $\Delta\varphi$-values as present for T ($CD\sim$ (0.15; 0.21) and $\Delta\varphi \sim 180°$). For the highest F_E, a similar behaviour as before, except for a fraction of MDA-MB-231, is recognized. In more detail, MDA-MB-231 show very low $\Delta\varphi$-values coupled with a highly elongated shape and a minor axis which lies in the observation plane, being strongly aligned with the flow (Fig. 16a). Such behaviour can be associated to TT ($CD\sim$ (0.21; 0.45) and $\Delta\varphi \sim 0°$). Referring to the motion regimes and looking at the highest applied F_E, we can easily appreciate that the major part of MCF-10A undergo a R motion (60%) whereas 50% of MCF-7 show T and 7% R motion. In the case of MDA-MB-231, 91% of cells show TT. It is clear how the classification is reliable, with a perfect matching of the mechanical and motion characteristics. Interesting differences in cell deformability emerge when correlating AR and CD with the previously mentioned dynamic parameters (Fig. 16d). In fact, MCF-10A and MCF-7 undergo R and T regimes, corresponding to the strengthening tendence observed in deformation, never reaching highly elongated shapes and then TT motions. Whereas, MDA-MB-231 appear to proportionally increase both in AR and
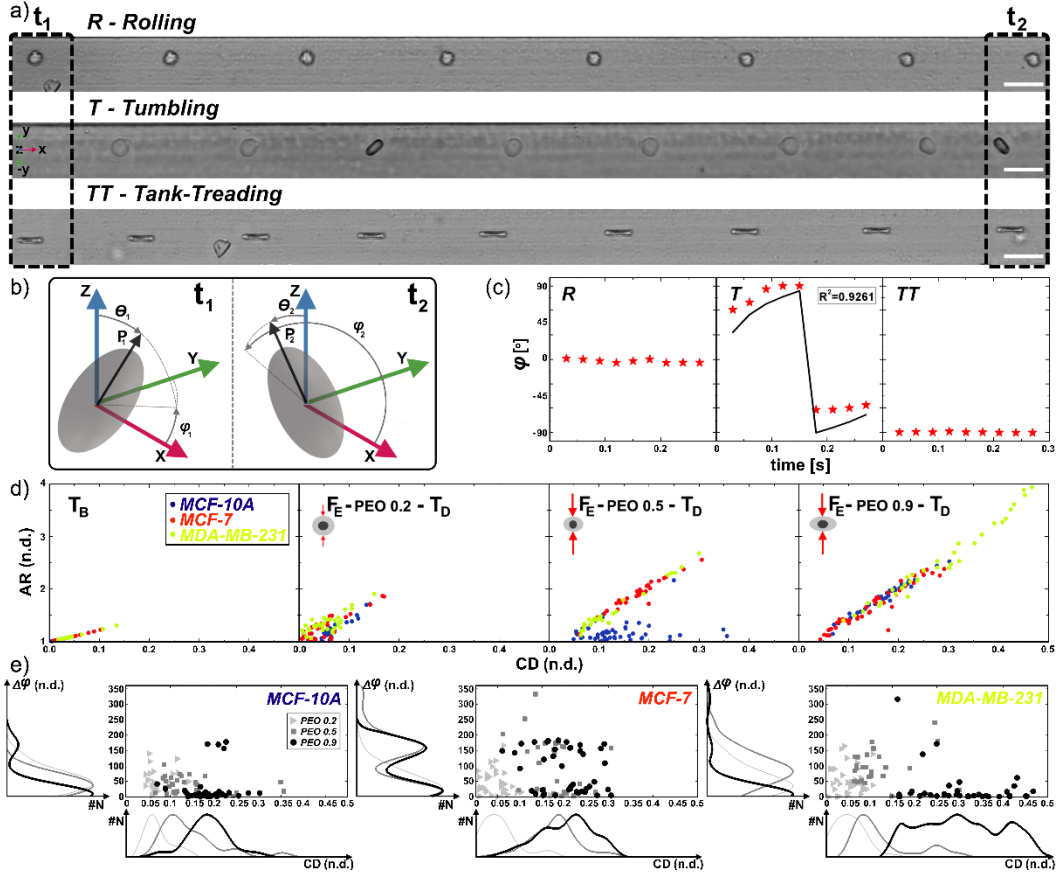
Fig. 16 Cell dynamics in-flow. a) Illustrative examples of cell dynamics in D (T_D) are shown. From the top, we report MCF-10A in PEO 0.5, MCF-7 in PEO 0.9 and MDA-MB-231 in PEO 0.9. Length of the scale bar is 50 μm. b) The reference systems for the dynamic cell rotation in-flow for two different time points. c) φ versus the observation time of the different cell dynamics presented in a) are presented. In the middle, a fitting curve of the Jeffery's orbit, for a representative MCF-7 cell is shown. d) *AR* versus *CD* results are plotted before- (T_B - PEO 0.9 with n=31, 29 and 19; F=3.49; p < 0.01) and after low- (T_D - PEO 0.2 with n=25, 33 and 35; F=7.97; p < 0.001), intermediate- (T_D - PEO 0.5 with n=50, 28 and 27; F=17.16; p < 0.001) or high- (T_D - PEO 0.9 with n=35, 42 and 35; F=10.24; p < 0.001 for MCF-10A, MCF-7 and MDA-MB-231, respectively) entities of in-flow applied F_E. Statistical significance has been determined by one-way MANOVA with Wilk's Lambda test. e) 3-D scatter plots of CD_{cell} versus $|\Delta\varphi|$ for all investigated PEO concentration (PEO 0.2 with n=25, 33 and 35; PEO 0.5 with n=50, 28 and 27; PEO 0.9 with n=35, 42 and 35; for MCF-10A, MCF-7 and MDA-MB-231, respectively) with corresponding histograms for *CD* and *Δφ*. Comparison of *CD* versus *Δφ* indicate possible ranges of cell motion.

CD, softening under the increasing forces and expressing a reciprocal variation among the three different dynamics (Fig. 16a and e). Histograms (Fig. 16e) distinctly show how three classes of motions, by increasing F_{EMax}, are depicted by different levels of deformation which, in turn, classify the cell line and distinguish them upon malignancy. This clearly defines the complete in-flow deformation-dependent dynamic motion signature with the strict interplay between $\Delta\varphi$, AR, CD and d_{Cell}.

In addition, at the exit of the microfluidic chip, a good cell viability was obtained for all cell lines, even at highest applied F_{EMax} (PEO 09).

3.3. Nuclear mechanical responses: from Lamin A/C alteration to chromatin re-organization.

Here, we succeed in monitoring substantial nuclear modifications in Lamin A/C expression and coverage, diffusion processes of probing molecules, YAP shuttling, chromatin re-organization and cGAS pathway activation as consequences of the applied in-flow compression. As a result, we show that high compression forces lead to a nuclear reinforcement (e.g. up to +20% in Lamin A/C coverage) or deconstruction (e.g. down to -45% in Lamin A/C coverage with a 30% reduction of chromatin condensation state parameter) up to cell death. We demonstrate how wide-range compression in microfluidics can be used as a tool to investigate nuclear mechanobiology and to define specific nuclear signatures for cell mechanical phenotyping.

3.3.1. Nuclear permeability changes upon different levels of in-flow compressive forces.

Previously shown in-flow deformation outcome (section 3.2.3) demonstrated that, for PEO 05 and PEO 09, MCF-10A and MCF-7 stiffen, whereas MDA-MB-231 tend to soften as the applied force increases. Such force-dependent behaviour was referred to the nucleus, as significantly more rigid in MCF-10A and MCF-7 compared to MDA-MB-231 [66]. As Lamin A/C is one of the major compartments involved in the mechanical cell nucleus deformation, we investigated Lamin A/C responses to different in-flow forces. According to force computation, bigger cells perceive higher compression forces with respect to smaller ones. Specifically, in our experiments, MCF-10A and MDA-MB-231 are similar in dimension, so they experience a comparable compression corresponding to ~20 µN and ~200 µN at PEO 05 and PEO 09, respectively (Fig. 17a). At Control, cell lines show different initial Lamin A/C expressions. Of interest, the increase of the Lamin A/C with the compression is faster in MCF-10A than in MCF-7 even though the entity of the perceived fluid force is higher for MCF-7, resulting in the maximum compression level (equal to 1), which corresponds to ~600 µN at PEO 09 (Fig. 17a). Thus, our results suggest that MCF-10A are more sensitive to the imposed compression (Fig. 17a and c).
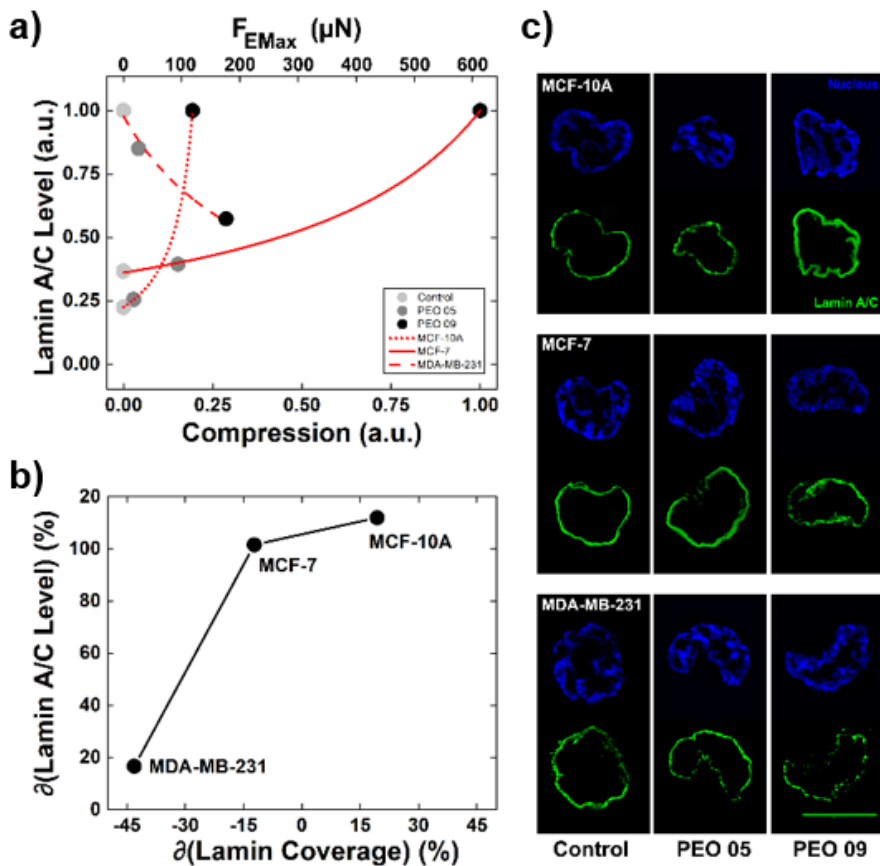
Fig. 17 Cell-dependent Lamin A/C changes after in-flow compressive forces. (a) Lamin A/C level expressed as normalized value of signal intensity on the maximum value reached by each cell line upon the different compression degree. The latter is defined as a normalized value of force with respect to the maximum applicable force into the microfluidic device, evaluated on the biggest size of cell that we test. A double x-axis helps in understanding the relationship existing between the non-dimensional applied compression and the estimated values of in-flow viscoelastic forces. MCF-10A result to be more sensitive to the applied compression than MCF-7, since the Lamin A/C protein level appears to be increased at PEO 09. On the contrary, MDA-MB-231 show a decreasing trend of the protein level as the force enhances. Fitting curves data: $1/((bx+a))$ with $a=4.43$ and $b=-17.76$ for MCF-10A; $a=2.77$ and $b=-1.77$ for MCF-7; $a=1.02$ and $b=2.64$ for MDA-MB-231. For all fitting curves, $R2>0.95$. (b) The variation values of the Lamin A/C level and coverage are reported in the case of PEO 09 compared to the Control condition for each cell line. As expected, increasing values of Lamin A/C level correspond to a greater coverage in MCF-10A, as well as decreasing protein levels coupled with a coverage disruption in MDA-MB-231. Interesting is the case of MCF-7 that enhance the Lamin A/C level but decrease in coverage content, possibly due to protein production phenomena. (c) Confocal images of

54

Lamin A/C and nucleus of the three cell lines tested in the three different experimental conditions are reported, highlighting the behaviour of increased coverage in MCF-10A (n=20, n=25, n=17 for Control, PEO 05 and PEO 09, respectively) and disruption in MCF-7 (n=25, n=26, n=23 for Control, PEO 05 and PEO 09, respectively) and MDA-MB-231 (n=26, n=19, n=16 for Control, PEO 05 and PEO 09, respectively), coupled with the correspondent level variations. Images are of the middle z-section of different nuclei. Scale bar: 5 μm.

Such evidence is also confirmed by a higher rate of variation of Lamin A/C level in MCF-10A with respect to the MCF-7, supporting the idea of a cell stiffening due to a more rigid nucleus of MCF-10A (Fig. 18). On the other hand, MDA-MB-231 show a decreasing Lamin A/C content in terms of signal intensity. We noticed, for MCF-10A, the enhanced expression level and coverage of Lamin A/C, possibly due to a recycling or a new production of the Lamin A/C protein as a consequence of the highest in-flow applied force. As expected, MCF-10A were characterized by typical wrinkles due to the induced non-adherent condition (Fig. 17c) [67]. On the contrary, with respect to the Control, MCF-7 slightly decrease in Lamin A/C coverage, despite the increase in the level amount. This response might be addressed to the necessity for the cell to produce new protein in order to activate a repair process of the impressed damage. A destroyed Lamin A/C is appreciable in the case of MDA-MB-231 that gradually deconstruct the structure, as the force increases, leading to a not recovered disruption (Fig. 17b and c, Appendix Fig. 1 and 2). In cancer cells, especially breast cells, it is known that lower levels of Lamin A/C correlate with a higher degree of metastatic potential [10, 17]. Thus, nuclei lacking Lamin A/C deform easier, allowing the invasion of the surrounding tissues.
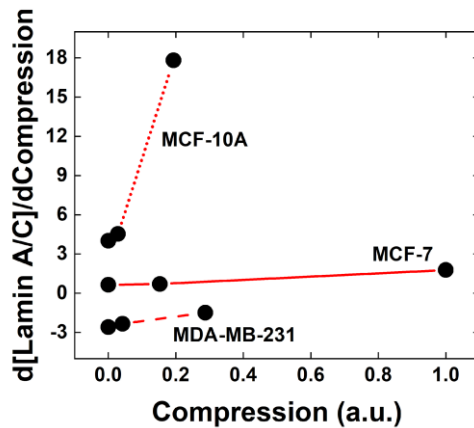
Fig. 18. Rate of change of Lamin A/C level. From the fitting curves used to describe the change of the Lamin A/C level, we derived the functions of rate of change of that quantity for each cell line. As we can see from the plot, MCF-10A increases more rapidly its own value of expression of the protein, despite of the lower applied loading condition since smaller sized than MCF-7. The latter seems to increase almost constantly in the Lamin A/C level. MDA-MB-231 represent a completely different case since its trend is a decreasing value of Lamin A/C protein.

However, a removal of Lamin A/C could lead to an increased cell death and then reduced metastasis. It has been demonstrated that, under elevated shear stresses conditions, MDA-MB-231 resulted to be more resistant to a shear force-induced apoptosis than MCF-10A, despite having a more compact and less deformable Lamin A/C than MDA-MB-231 [68]. We hypothesize that, under in-flow compression, the cellular response changes by reversing the trend, with MCF-10A more resistant than MDA-MB-231, at the Lamin A/C level. On this line, we tested cell vitality by observing how the recovered cells after the in-flow compression adhere on a plastic substrate (~ 2 GPa) (Fig. 19). For each line and applied force, after at least 3 hours of adhesion, cells spread on the substrate, except for MDA-MB-231 at the highest compression. This suggests a not recovering of the functional cell activities, mainly due to a not reversible Lamin A/C damage that triggers a

cell death process. Previous studies demonstrated that in MDA-MB-231, a suspension state increased the adhesion and the cytoskeleton formation, as a consequence of Lamin A/C up-regulation [69]. These findings suggest that, although the suspension state, our applied in-flow forces inhibit MDA-MB-231 adhesion after Lamin A/C rupture and reduced level expression. Different is the case of MCF-7 that respond after the in-flow forces by recovering their own functional vitality although the noticed Lamin A/C damages.
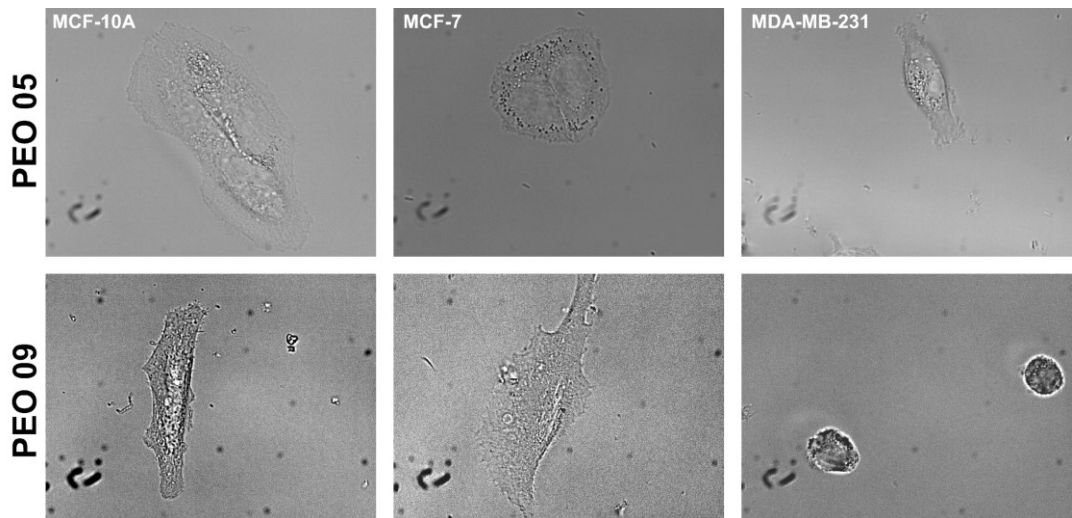

Fig. 19 Cell vitality images. Vitality images of reattached cells after in-flow PEO 05 and PEO 09 conditions. Alive cells have been observed after at least 3 h of attachment. No functional recovering is observed in MDA-MB-231 at PEO 09.

In recent years, it has been demonstrated that a direct force application on the nucleus leads to an increased YAP influx into the nucleus. To study whether our in-flow compression generates similar cell responses, we investigated YAP nuclear signal. In Control, all of the three cell lines express a well-defined YAP cytoplasmic signal (Fig. 20a, b and c, on the top).

Both MCF-10A and MCF-7, at PEO 05, show not altered Nuc/Cyt ratio and Lamin A/C coverage. Scatter plots highlight cell-specific trends of response (Fig. 20a, b and c, on the top). In fact, MCF-10A at PEO 09 show an evident increase of the YAP Nuc/Cyt-ratio as well as of the Lamin A/C content (Fig. 20a, on the bottom and Appendix Fig. 3). Particularly, the shuttling of mechanosensitive YAP suggests that a thickening and an enhancement of the Lamin A/C content regulate the nuclear expression of the transcription factor, with a two-fold increase of YAP signal after the in-flow compression. It is known that, on stiff substrates, cells with high expression levels of Lamin A/C present a higher nuclear YAP content, suggesting that the Lamin A/C changes influence nuclear localization of transcription factors [14, 68]. Thus, similar effects are appreciable by inducing a cell deformation up to the nucleus level in our conditions.

MCF-7 show a different scenario, instead. The YAP Nuc/Cyt-ratio increases, defining a shuttling phenomenon due to a double effect of mechano-regulated response and enhanced nuclear permeability at the ruptures' localization of the Lamin A/C. In fact, scatter plots show a shifting at lower levels of coverage corresponding to higher values of Nuc/Cyt-ratio, suggesting that some points of damage are present at the Lamin A/C level favouriting the molecule re-localization (Fig. 20b, on the bottom and Appendix Fig. 3). However, previous studies described YAP protein levels as decreasing with Lamin A/C knockdown and then with the relative NE losses [14, 68]. MDA-MB-231 outcome show decreasing or unaltered values of YAP Nuc/Cyt-ratio at PEO 09, with Lamin A/C deconstruction.
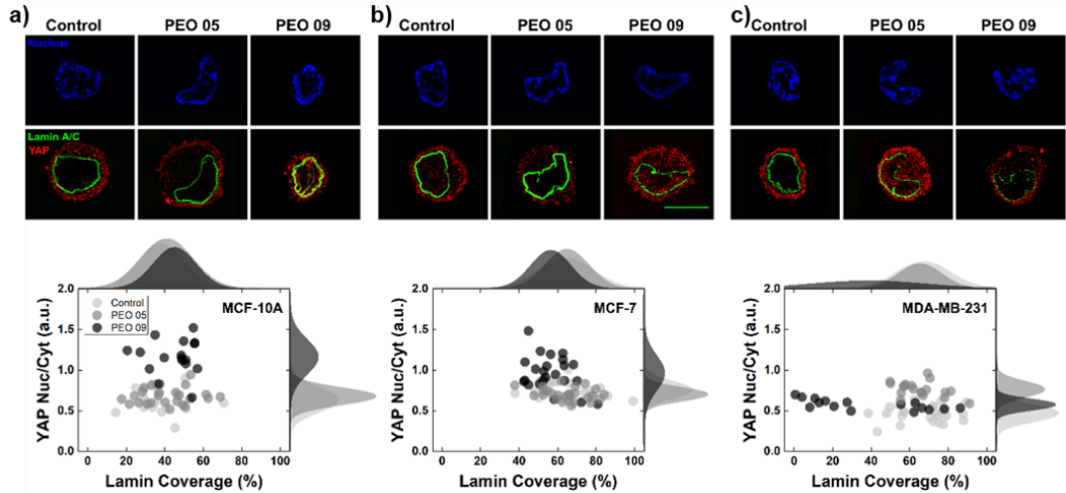
Fig. 20 YAP shuttling phenomena associated to Lamin A/C changes. a) On the top, confocal images of Lamin A/C (green) and YAP (red) in MCF-10A tested in the three different experimental conditions are reported, highlighting the behavior of increased coverage and gradual YAP nuclear content increment up to PEO 09. On the bottom, a scatter plot representation of the YAP Nuc/Cyt-ratio with respect to Lamin A/C coverage is reported describing how no relevant changes are expected at PEO 05 but only in the higher values of the parameters at PEO 09 with respect to the Control condition (n=20, n=25, n=17 for Control, PEO 05 and PEO 09, respectively). b) On the top, confocal images of Lamin A/C and YAP in MCF-7 tested in the three different experimental conditions are reported, highlighting that Lamin A/C slightly decreases in Coverage while YAP nuclear content enhances at PEO 09. On the bottom, a scatter plot representation of the YAP Nuc/Cyt-ratio with respect to Lamin A/C coverage confirms how a competition between a mechanosensitive process and an increasing of the YAP nuclear signal due to an enhanced nucleus permeability is possible, at PEO 09 condition (n=25, n=26, n=23 for Control, PEO 05 and PEO 09, respectively). c) On the top, confocal images of Lamin A/C and YAP in MDA-MB-231 tested in the three different experimental conditions are reported, showing that Lamin A/C coverage decreases as well as the YAP signal, at the highest PEO concentration. Differently, at PEO 05, a competitive mechanism for the increasing YAP Nuc/Cyt-ratio, as described for MCF-7, is appreciable. Such outcome are confirmed by the scatter plot representation, reported on the bottom (n=26, n=19, n=16 for Control, PEO 05 and PEO 09, respectively). Images are of the middle z-section of different nuclei. Scale bar: 5 μm.

Therefore, the MDA-MB-231 inability to mechanosense the applied compression and to perform a YAP shuttling phenomenon might be

ascribable to a loss in cell vitality. Conversely, at PEO 05, MDA-MB-231 behave like MFC-7, by slightly decreasing in Lamin A/C coverage but with a small increase in YAP Nuc/Cyt-ratio (Fig. 20c, on the bottom and Appendix Fig. 3). Further, the mentioned phenomena might be attributed to a variation of the mechanical stability and/or molecular weight of YAP if bound/unbound to other molecules [23].

To test whether, in our conditions, the reduction of Lamin A/C coverage promotes an enhanced nuclear permeability, we measured and analysed the nuclear entry of the Hoechst 33342 molecules. After having recovered cell samples subjected to the in-flow compression, they were directly fixed to evaluate the kinetics of Hoechst from the cytoplasm to the nucleus. In detail, after loading the Hoechst solution in contact with the cell sample, we monitored the kinetics of molecule entry for 10 minutes, to reduce undesired cell movements, saturation, or bleaching signal events. At Control, the Hoechst entry kinetics is cell-line dependent resulting both in different velocity and intensity levels reached during the phenomenon (Fig. 21a, Control). In particular, MCF-10A do not show relevant differences between Control and PEO 05, since both the intensity and the entry behaviour remain unaltered after compression (Fig. 21b-MCF-10A, Appendix Fig. 4, Table 4). At PEO 09 we observe a hindered passage of the Hoechst into the nucleus, due to the previously described Lamin A/C thickening, leading to a drastic reduction of the final nucleus intensity. MCF-7, instead, show an enhanced Hoechst mobility, particularly at PEO 09,
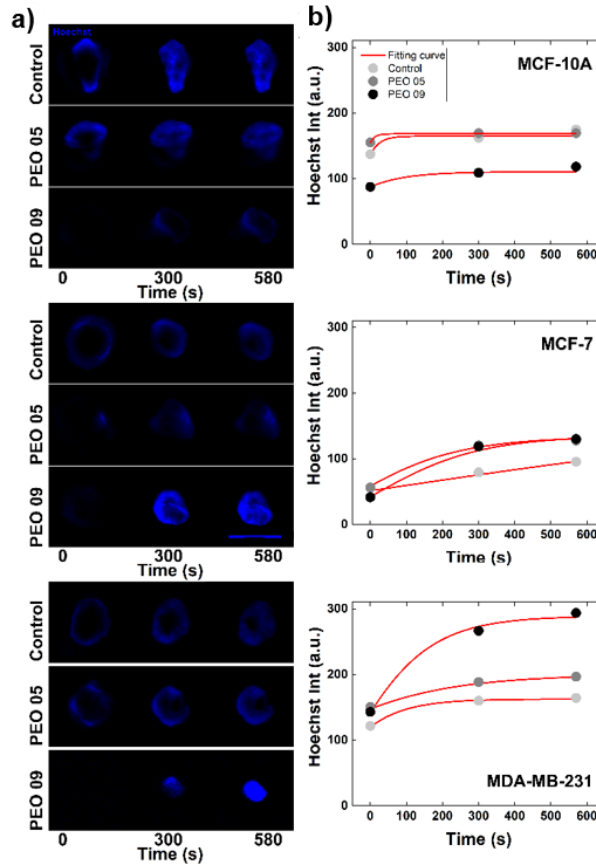
Fig. 21 Recording Hoechst molecule entry into the cell nucleus reveals an enhanced nuclear permeability after in-flow compression. (a) Microscope images of cell nuclei stained with Hoechst 33342 solution at three time points (0, 300, 580s) of the entire kinetics of Hoechst entry for a total period of 10 minutes. On the left, MCF-10A show that, at PEO 09, Hoechst nuclear delivery from the cytoplasm to the nucleus is hindered by the thicker Lamin A/C. In the middle, MCF-7 are represented. Both at PEO 05 and PEO 09 the nuclear influx is enhanced by the Lamin A/C changes, with a difference in the final reached intensity level that appears to be higher in the case of PEO 09. On the right, MDA-MB-231 gradually increase in nuclear Hoechst influx, reaching maximum values of both entrance velocity and final intensity level at PEO 09. (b) Fitting curves by application of Gompertz model are shown. In MCF-10A, at PEO 09 (n=5, n=4 and n=5 at Control, PEO 05 and PEO 09, respectively), Hoechst intensity level clearly reduces in comparison with the Control condition, whereas MCF-7 (n=7, n=5 and n=5 at Control, PEO 05 and PEO 09, respectively) and MDA-MB-231(n=7, n=4 and n=7 at Control, PEO 05 and PEO 09, respectively) speed up the entry reaching higher levels of final intensity both at PEO 05 and PEO 09. MDA-MB-231 reach a twofold higher intensity value at PEO 09 with respect to Control. Scale bar: 5 μm.

where localized ruptures of the Lamin A/C allow for a facilitated passage of external molecules. However, similar variations on the final Hoechst nuclear intensity are present at PEO 05 and PEO 09 conditions (Fig. 21b-MCF-7, Appendix Fig. 4, Table 4).

The Hoechst kinetics results to be completely altered by the in-flow compression for MDA-MB-231. We observe a gradual increase of the Hoechst signal, clearly enabled by the Lamin A/C deconstruction which already starts at PEO 05 compression. A facilitated movement of the molecule is then possible thanks to an increased permeability. However, an almost saturated signal is observed at the last time point of the experiment at PEO 09 (Fig. 21b-MDA-MB-231, Appendix Fig. 4, Table 4).

Table 4 Fitting parameters of Hoechst dynamic entry into cell nucleus at Control, PEO 05 and PEO 09 condition. The used fitting curve is a Gompertz model: $Aexp(-exp(-B(x-c)))$ where x is the time and c the time fitting parameter. For all fitting curves, $R^2>0.75$.

Cell Type	Plateau Intensity (A) (a.u.)	Growth rate (B) (s)
MCF-10A - Control	164.88	0.0410
MCF-10A - PEO 05	168.42	0.0880
MCF-10A - PEO 09	110.56	0.0110
MCF-7 - Control	166.64	0.0013
MCF-7 - PEO 05	133.60	0.0062
MCF-7 - PEO 09	135.79	0.0061
MDA-MB-231 - Control	162.48	0.0110
MDA-MB-231 - PEO 05	200.05	0.0048
MDA-MB-231 - PEO 09	288.90	0.0084

3.3.2. Chromatin condensation reduction relates to nuclear permeability changes, revealing cGAS cytoplasmic activity.

Within the nucleus, Lamin A/C regulates DNA replication and repair as well as chromatin organization. In particular, heterochromatin exists at the nuclear periphery and interacts with the nuclear Lamin A/C at specific sites. These interactions may directly affect chromatin organization, nucleus mechanosensitivity and then, transcriptional activity [10,70-72]. For this reason, observing the changes of Lamin A/C at the various degrees of applied in-flow compression, we asked whether these modifications also translate at the level of nucleus with alterations of chromatin condensation. Lamin A/C thickening does not confer a higher chromatin condensation to the nucleus in MCF-10A (Fig. 22a, on the top). Scatter plots and relative mean values of chromatin condensation parameter (CCP) show not relevant modifications at the chromatin level are present at the two in-flow compression conditions (Fig. 22a, on the bottom and Appendix Fig. 5). Similar for MCF-7, despite a different chromatin content already at the Control condition (Fig. 22a, on the bottom and Appendix Fig. 5). A decreasing trend of chromatin condensation is observed in MDA-MB-231, which can be associated with previous Hoechst molecule outcome. In fact, chromatin density and condensation affect the nuclear influx of molecules sized up to ~30 kDa, hindering or slowing down the passage of bigger molecules like Hoechst as well [73].
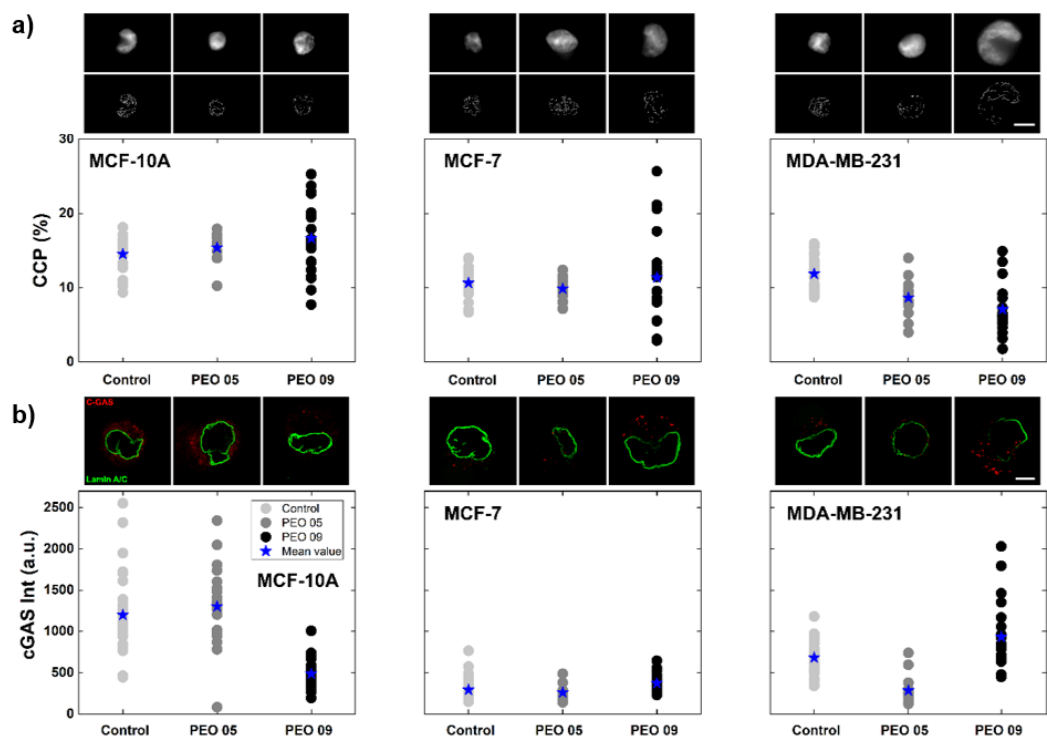
Fig. 22 Chromatin condensation changes and cGAS localization on DNA damages are correlated with Lamin A/C ruptures. (a) Chromatin microscope fluorescent images and scatter data of CCP are presented for each cell line at the three different measurement conditions. MCF-10A and MCF-7 do not show relevant CCP changes, while MDA-MB-231 gradually decrease in chromatin condensation by increasing the applied compression (MCF-10A: n=31, n=10, n=25 at Control, PEO 05 and PEO 09 respectively; MCF-7: n=20, n=13 and n=20 at Control, PEO 05 and PEO 09, respectively; MDA-MB-231: n=26, n=18 and n=20 at Control, PEO 05 and PEO 09, respectively). (b) cGAS intensity is reported for each cell line in the three different measurement conditions, as probing tool to verify whether a chromatin de-condensation and the DNA damages occur once the Lamin A/C ruptures. On the top, cGAS confocal images show a scattered initial signal into the cell cytoplasm without specific localization at DNA spots. This results to be evident at PEO 09 in MCF-7 and MDA-MB-231, whereas cGAS signal content decreases in MCF-10A at PEO 09 and MDA-MB-231 at PEO 05. On the bottom, scatter data plots confirm the aforementioned trends of modification (MCF-10A: n=34, n=21, n=30 at Control, PEO 05 and PEO 09 respectively; MCF-7: n=39, n=10 and n=31 at Control, PEO 05 and PEO 09, respectively; MDA-MB-231: n=32, n=18 and n=25 at Control, PEO 05 and PEO 09, respectively).

However, Lamin A/C ruptures coupled with chromatin losses reveal possible reasons for the MDA-MB-231 failure in vitality. Scatter plots clearly indicate the highest decrease of chromatin content at PEO 09 condition. To test whether chromatin losses coupled with DNA exit into the cytoplasmic region, we evaluated the activation of cGAS protein, which is a fundamental cytosolic DNA-sensor [74,75]. At Control condition, cell lines express a cGAS quote into the cytoplasm (Fig. 22b, on the top) due to the fact that cGAS is localized in the cytoplasm of nondividing cells but it associates to DNA foci once an accumulation of damaged DNA into the cytoplasm occurs. However, scattered signals of cGAS without specific localization with DNA spots are present in our Control condition (Fig. 22b, on the top). We observed that not relevant modifications in the scatter data and mean values of cGAS intensity are present in MCF-10A and MCF-7 after in-flow compression at PEO 05 (Fig. 22b, on the bottom and Appendix Fig. 6). Of note, at PEO 09, MCF-10A show a decreasing level of cGAS intensity, which suggests that a possible protein content modification has occurred. A similar result is present at PEO 05 in MDA-MB-231. At PEO 09, well-defined spots of active cGAS attached on damaged DNA are present in MCF-7 and MDA-MB-231. The latter shows that such cGAS content colocalizes or results to be close to the Lamin A/C ruptures. cGAS further confirmed that Lamin A/C damages occurred at the highest compression conditions opening the nucleus to the cytoplasmic side and relative induced pathways. Remarkably, the substantial enhancement of cytosolic cGAS expression may restrain DNA repair and evoke cell death, as observed in MDA-MB-231 at PEO 09 condition [75].

3.4. Actin Cortex and Microtubule remodelling.

In this section, we introduce the major cellular components involved into mechanical responses, trying to understand how each of these cooperates also to the previously shown nuclear envelope and chromatin modifications. Thus, comprehending the dynamics and mechanics of the cellular components is prerequisite to explain the molecular origins of cell mechanical properties. We show that, at high compression, the most responsive component is the actin cortex. Both structural and expression modifications are appreciable, with either a cortex ring fragmentation or an enhancement of the intensity signal if a protein production occurs. Interesting results demonstrate that the drug effects of Cytochalasin-D (CYTD) and Nocodazole (NOCO) applied on cells in Control condition, lead to similar configuration changes of the two structures appreciable after PEO 09 application on untreated cells.

3.4.1. Actin Cortex and Microtubule role in cell deformation.

In suspension, cells develop a well-defined spherical geometry free of visible stress fibers with the actin cytoskeleton forming a cortex structure which spans the entire cell [76]. Instead, the microtubule network presents as random at the cell interior while with pronounced bundles at the periphery [77]. This aligned peripheral bundling may be due to collective buckling at the cell's boundary. However, it is well know that depending on the loading entity actin cortex and microtubules respond differently. Our outcome about cell deformability responses (section 3.2.3) show a large deformation regime (deformation > 5%) for all of the three cell lines at PEO 09. Furthermore, being nuclear permeability highly affected at this high compression condition, we decided to test actin cortex and microtubule

66

condition in the range of 100-1000 µN. In fact, at large deformation, actin constituents have been shown to rupture while microtubule network to elastically respond [77].
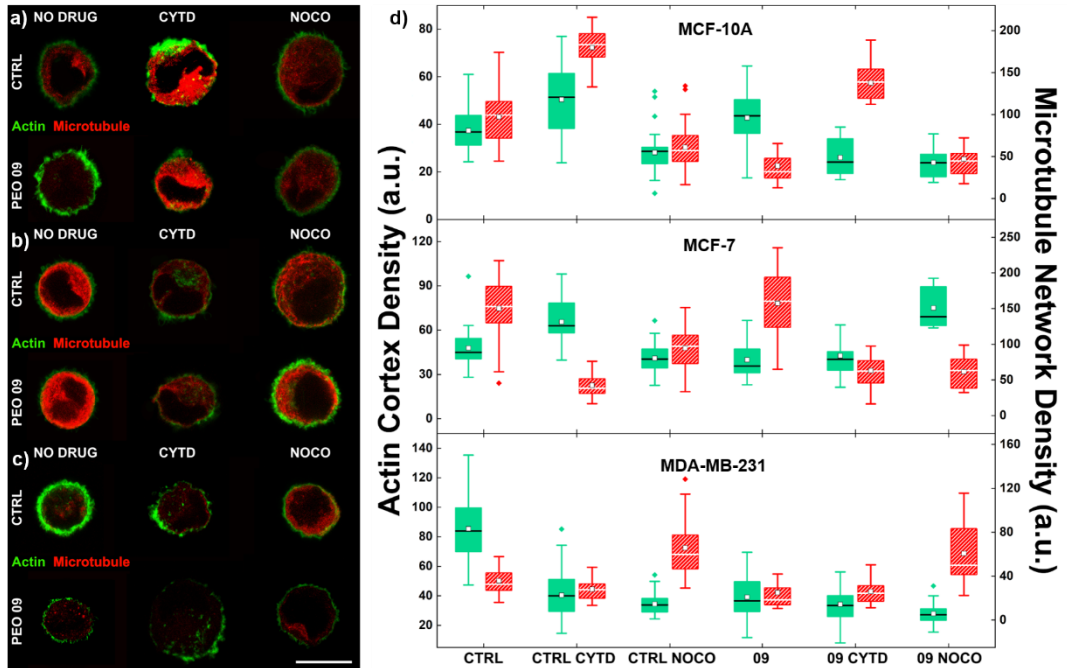

Fig. 23 Actin Cortex and Microtubule Network assembly and disassembly after in-flow compression. a) MCF-10A confocal images represent actin cortex (green) and microtubule network (red), at CTRL and PEO 09 both with untreated and treated cell samples. Relevant changes are appreciable between CTRL and PEO 09 as well as among the three CTRL conditions, both at the actin and the microtubule levels (CTRL n=28, PEO 09 n=35; CTRL CYTD n=30, PEO 09 CYTD n=18; CTRL NOCO n=37, PEO 09 NOCO n=31). b) MCF-7 images reveal a more sensitive response to the drug treatment, as for the actin cortex as for the microtubule network, especially in the case of the NOCO drug (CTRL n=27, PEO 09 n=24; CTRL CYTD n=25, PEO 09 CYTD n=21; CTRL NOCO n=28, PEO 09 NOCO n=8). c) MDA-MB-231 show an initial thick and structured cortex which decreases both after treatment and after PEO 09. Microtubules do not undergo relevant modifications (CTRL n=27, PEO 09 n=33; CTRL CYTD n=28, PEO 09 CYTD n=33; CTRL NOCO n=31, PEO 09 NOCO n=25). Images are of the middle z-section of cells. Scale bar: 5 µm. d) The normalized values of intensities of the actin and microtubule signals are reported for each condition. The statistical analysis is reported in Table 5 in Appendix A.

Particularly, actin responses depict the nonlinear behaviour of cells as strain stiffening or strain softening. At CTRL, both actin cortex and microtubule network configuration is cell line dependent. For this reason we compared the obtained results among the two experimental conditions for each cell line.

MCF10-A show a compact actin cortex ring at CTRL in untreated condition (Fig. 23a). Instead, microtubules form a random network with highly concentrated regions in correspondence of the nucleus. With CYTD drug, the intensity of both actin and microtubules appears to be higher than the untreated state (Fig. 23a), possibly because cells try to recover their own structure after the treatment, producing new protein. However, the ring structure appears highly fragmented confirming the effects of the applied drug (Fig. 24a and c). From PEO 09, such fragmentation results to be different since points of accumulation of actin with high intensity are present. In fact the sum of areas present all along the actin structure is the highest always at the ring confinement, while at PEO 09 such fragments area distribution spans over the entire spatial organization as well (Fig. 24a). Interestingly, at PEO 09, a trend of increasing actin signal intensity is appreciable exactly like in the case of Lamin A/C at the nucleus level (Fig. 23d-MCF-10A). In adhesive condition, it has been previously demonstrated that that Lamin A/C and the Actomyosin system monotonically increase in protein levels expression, with substrate rigidities [14]. Thus, our outcome confirm that, despite the absence of a physical link between the NE and a well-structured cytoskeleton, a mechanosensitive response of the nucleus is present for MCF-10A after the imposition of in-flow compression conferring recycling or
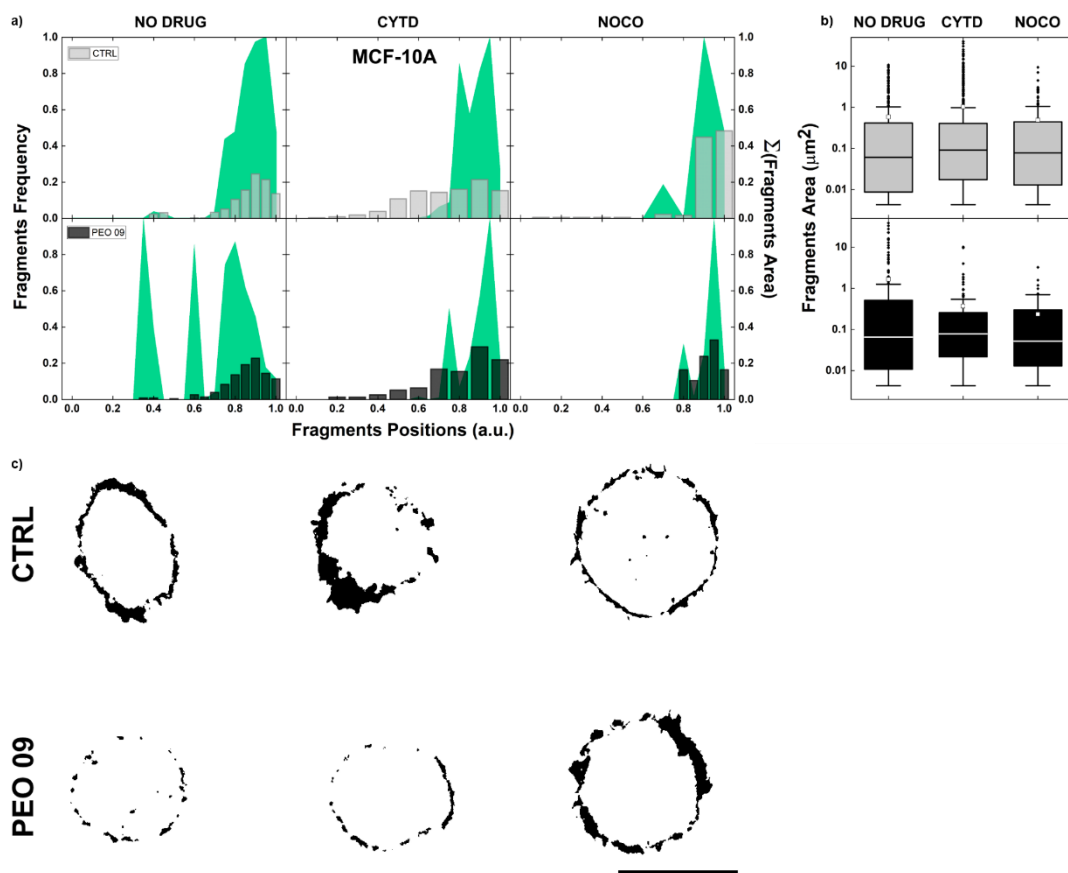
68

Fig. 24 Actin fragments characterization after in-flow compression for MCF-10A. a) Light grey and black histograms represent the fragment distribution as position, near and far from the cortex ring, at CTRL and PEO 09 for untreated and treated cells respectively. In green, the summation of fragments area is presented. In particular, each bin of the fragments position data is specified by the respective summation of areas in order to understand where the major areas are localized. Compact actin cortex is present at untreated CTRL and with NOCO drug. At untreated PEO 09, the structure is changing, with fragments area distributed differently from the CTRL condition, appearing to be present also far from the ring. Broken actin cortex, instead, is present after CYTD treatment, without relevant changes after the in-flow compression. b) Box chart representation of the fragments area. Not relevant alterations are present among the different conditions. c) Threshold images of the actin cortex to identify the constituent fragments. Statistical analysis of fragments position and areas is reported in Table 6 and Table 7 (Appendix A). Scale bar: 5 µm.

production phenomena of proteins of interest. Moreover, the intensity increasing reached at PEO 09 is present also at CTRL CYTD, as if the effect of the in-flow compression was comparable to that of the drug. Whereas, microtubules intensity decreases in all of the PEO 09 condition, as treated or untreated with the respective CTRL, suggesting a reduction in concentration of the network (Fig 23a and d-MCF10A).

Completely different is the case of MCF-7. Surprisingly, not relevant modifications of the two structures are evident. In fact, actin cortex fragmentation does not change (Fig. 25a) except for the PEO 09 NOCO condition at which we observe a qualitative trend of cortex ruptures but that is not statistically significant. Although the content of microtubules decreases mainly with the application of NOCO, they seem to constitute a cortex-like structure at the periphery of the cell (Fig. 23b and d-MCF-7). How, during the deformation process, an interplay between actin cortex and microtubule could cooperate for Lamin A/C localized ruptures and thus to an increased nuclear permeability (section 3.3.2) is still not clear. It is possible that the reason is in the size of the nucleus and of the cell itself. As already mentioned in the previous section (2.3.2), MCF7 is possible to strengthen at high compression levels. This can be explained by a higher nucleo-cytoplasmic ratio compared to that of the MCF-10A [7] and also by the fact that they perceive the highest force being on average larger than the other cell lines. However, a decrease in the actin cortex density is present between CYTD conditions, CTRL and PEO 09. On the contrary, an increase of the actin signal is appreciable at PEO 09 NOCO compared to its own CTRL.
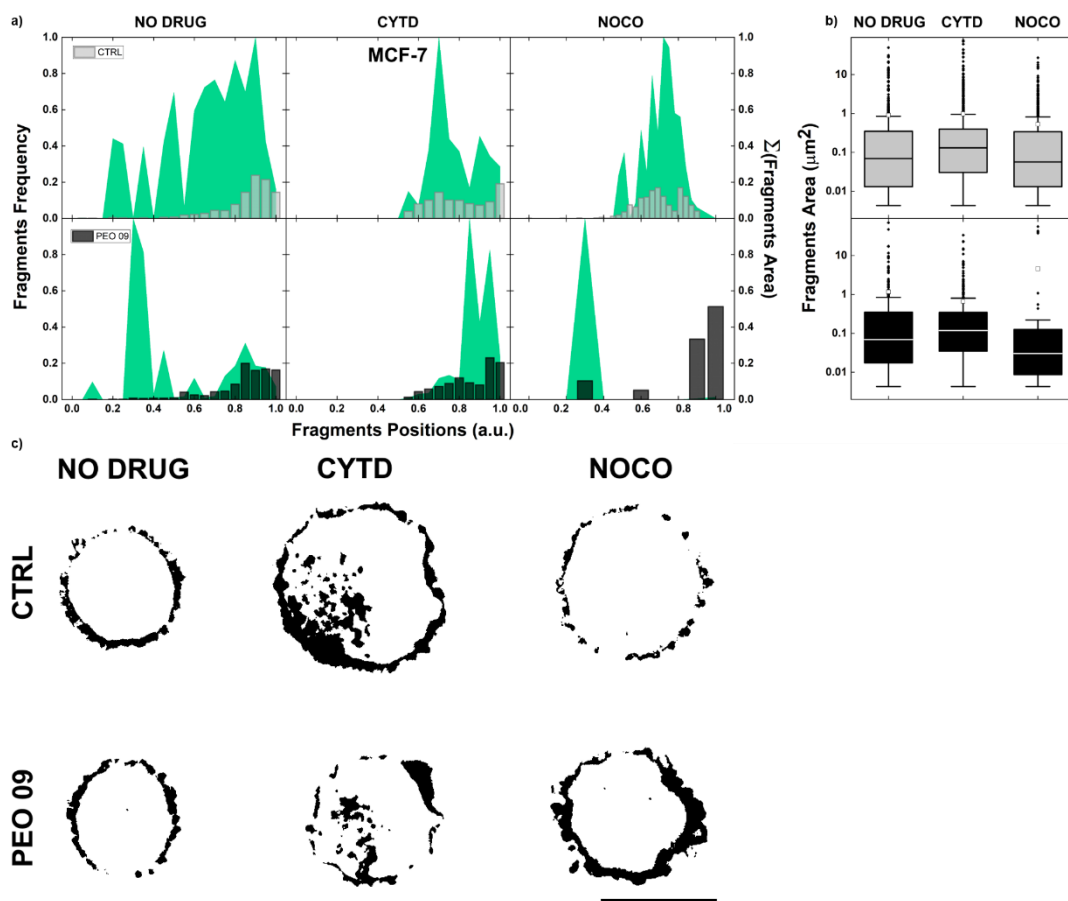
Fig. 25 Actin fragments characterization after in-flow compression for MCF-7. a) Looking at the fragments position distributions, not relevant alterations are present between the CTRL conditions and the relative PEO 09. Drug effects are appreciable still into the CTRL. An interesting trend in fragmentation of the actin cortex is shown in PEO 09 NOCO, where a not regular distribution of fragments occurs. b) Box chart representation of the fragments area. Not relevant alterations are present among the different conditions. c) Threshold images of the actin cortex to identify the constituent fragments. Statistical analysis of fragments position and areas is reported in Table 6 and Table 7 (Appendix A). Scale bar: 5 μm.

MDA-MB-231 reveal interesting responses, both at actin and microtubule level. A decreasing of the densities as well as of the compaction degree of the actin cortex is recorded, for CTRL condition of treated and untreated cells

(Fig. 23a and d-MDA-MB-231). Except for CTRL NOCO, where an increasing microtubule density is observed due to the peripheral points of accumulation already seen for MCF-7. At PEO 09, the resulting actin signal is comparable with the one observed at CTRL CYTD, suggesting similar effects coming from the drug application and the in-flow compression. No further changes at the actin cortex levels occur at PEO 09 CYTD (Fig. 23c and d-MDA-MB-231). The fragmentation phenomenon at PEO 09 suggests a possible explanation also to the critical Lamin A/C deconstruction with consequent cell death. In adhesive conditions, it has been shown that the alteration in microtubule organization upon actin perturbation results in nuclear elongation, which was related to altered conformations of Lamin A/C [78]. In our case, we demonstrate that after the in-flow compression the actin cortex is partially re-organized with lower signal intensity and fragments position. At the microtubule level a slight decreasing of the intensity level occurs coupled with a spot-like distribution of such signal into the cell interior like defining accumulation points of microtubules near the nucleus. Then, it is reasonable that such actin and microtubule perturbation could be translated into the Lamin A/C deconstruction observed at PEO 09. Actually, actin density reduction occurs in each PEO 09 for untreated or untreated cells, with the same trend. More compact actin cortex is shown at PEO 09 NOCO (Fig. 26a and c), with not relevant microtubule modifications.
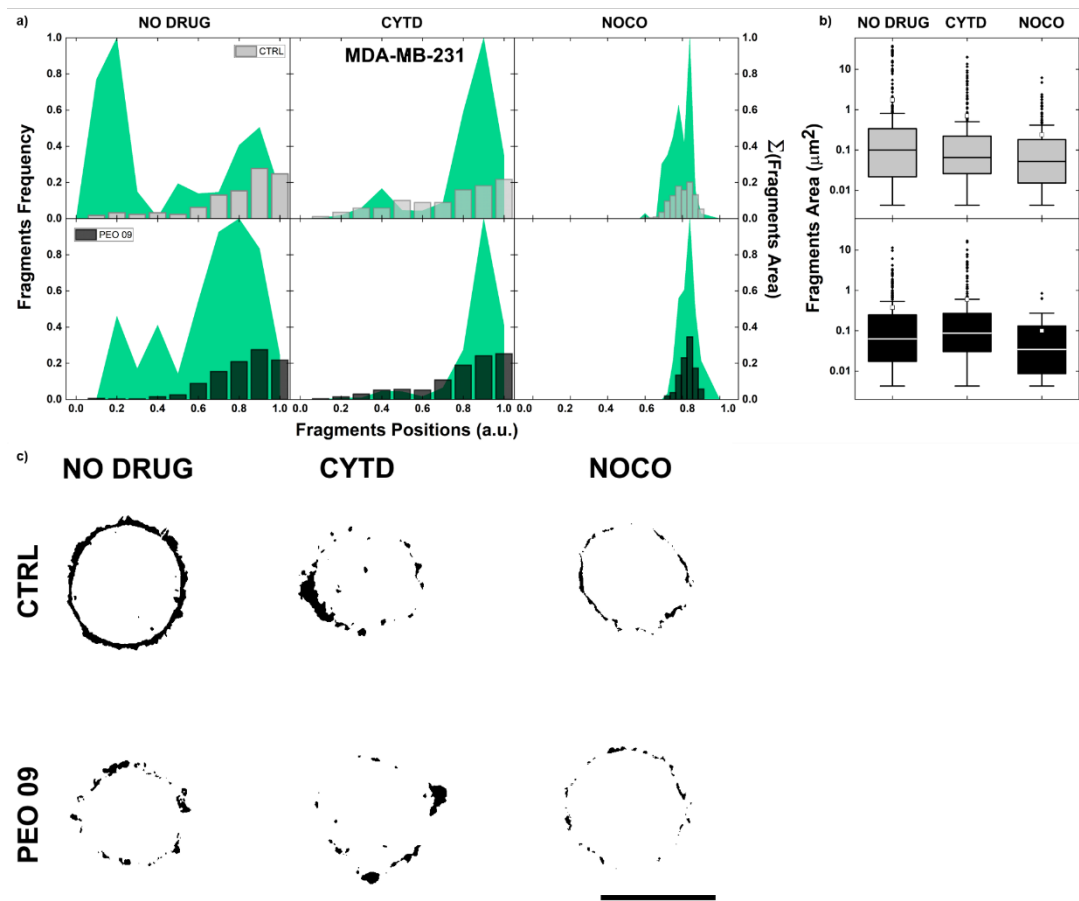
Fig. 26 Actin fragments characterization after in-flow compression for MDA-MB-231. a) Looking at the fragments position distributions, not relevant alterations are present between the CTRL conditions and the relative PEO 09. Drug effects are appreciable still into the CTRL. Both at PEO CYTD and NOCO, the actin cortex appears to be more compact both as fragments position and areas. b) Box chart representation of the fragments area. Not relevant alterations are present among the different conditions. c) Threshold images of the actin cortex to identify the constituent fragments. Statistical analysis of fragments position and areas is reported in Table 6 and Table 7 (Appendix A). Scale bar: 5 µm.

4. Conclusions and Future Perspectives

4.1. Cell dependent mechanobiological responses.

The presented microfluidic approach, based on tuneable compressive forces, is a simple tool to rapidly deform cells up to the nucleus level for phenotyping different cell lines. The microfluidic chip results to be simple in force calibration, making it highly suitable for biological experiments. Our fluid-flow induced forces arise from a viscoelastic medium, flowing into a sequence of variable microfluidic cross-sections. By simply changing the viscoelastic properties and the initial velocity conditions, we are able to apply tuneable compressive forces over a wide range (10-10^3 µN), which directly lead to different degrees of cell deformation. The microfluidic approach is able to provide aarisen interesting coupling between the classical deformation parameters that describe morphological and shape alterations with respect to dynamic quantities. In fact, a backward analysis of cell deformability, starting from the motion to get the mechanical property, is possible. By properly calibrating the fluid dynamic conditions and the viscoelastic forces, the microfluidic chip allows to provide a cell type characterization simply based on i) orientation angle, ii) aspect ratio, iii) cell deformation and iv) cell diameter. The combination of this set of parameters leads to a mechanical signature of any cell line has to be analysed. Furthermore, the resulting in-flow nucleus deformation brings out the possibility to activate pathways and responses generally ascribable to adhesive and migratory cell behaviour. Particularly, compressive forces offer the possibility to calibrate both cell-specific cytoskeletal and nucleus mechanical responses causing losses in structural integrity, triggering

74

mechanosensing reactions or favouring enhanced nuclear permeability as well as chromatin re-organization. Based on nuclear deformation outcome, our approach proposes as a new tool for enhanced nuclear delivery of probing molecules, possibly reducing time of analysis and classical staining procedures, based on chemical permeabilization.

The presented on-chip and off-chip outcome are not only useful for breast cell lines, since the microfluidic device is well-suited to analyse the mechanical phenotype of other cell types, such as circulating tumour cells or immune system cells also as mixed samples. A next step of analysis would be the implementation of a mathematical model able to comprehensibly describe cell mechanics behaviour, starting from grouping morphological and dynamic in-flow parameters and then coupling them with the extracted characteristics of inner cell structures, analysed in quiescent conditions. Of course, such a kind of model could be of interest also to correlate the obtained modulation of cytoskeletal and nuclear responses to those conventionally associated to adhesive and migratory cell behaviour.

On this line, for future investigation, we want to demonstrate that the highest compression is able not only to promote an increased nuclear permeability, but also to favour a greater efficiency of nanoparticles intracellular delivery. In fact, we show how such delivery is possible escaping the physiological endocytosis and only relying on reversible ruptures of the plasma membrane after the applied in-flow compression. In the next section we illustrate an example experimental case on MCF-7.

4.2. Future Perspectives: the intracellular delivery across mechanically disrupted Plasma Membrane.

During last years, an increasing research interest arose about the possibility to induce enhanced intracellular delivery of exogenous material across the plasma membrane by escaping the physiological endocytic pathways. In general, as transport mechanisms, we can distinguish carrier-mediated methods which comprises endocytic and fusion entry pathways, and membrane disruption-based intracellular delivery, which includes direct penetration and plasma membrane permeabilization mechanisms [79]. Four mechanisms are ascribable for intracellular delivery: (1) permeabilization, (2) penetration, (3) endocytosis, and (4) fusion. Such mechanisms can overlap on more than one mechanism possible promoting an intracellular delivery via multiple pathways depending on the context [79-81]. In general, membrane disruption refers to the generation of any hole that would increase the permeability of the plasma membrane to cargo, by means of possible multiple perforations of all sizes and shapes. The plasma membrane is considered permeable when membrane disruptions are of sufficient size and lifetime to permit passage of the cargo molecules [79]. Upon membrane disruption the cell responds with active membrane repair processes that can take from a few seconds up to several minutes to complete. Once membrane integrity is restored, the cell active processes to restore membrane and cytoplasmic environment. It may take hours for the cell to return to the perturbation state [82]. Crucial factors that influence plasma membrane repair and then delivery efficiency are calcium composition of the buffer, temperature, and incubation time post-treatment [79-83]. Particularly, temperature highly affects endocytic processes since it

is known that cooling a cell culture to 4°C slows down intracellular delivery mechanisms [84]. However, efficiency and good viability of cells after membrane-disruption events are still challenging goals for current available techniques, like electroporation, confined geometries or sonoporation.

Here, we show how in-flow compressive forces lead to transient plasma-membrane ruptures which provide a not endocytic-mediated delivery mechanism into the cell. In fact, we show that at PEO 09 a temporary membrane disruption could occur, allowing to an intracellular delivery of carboxylate nanoparticles (NPs) of 200 nm and 1 µm. Escaping endocytosis is demonstrated by the fact that such delivery has been tested in freezing conditions, placing the cells at 4°C after the in-flow deformation and then inhibiting the active processes possibly related to the NPs entry.

4.2.1. Preliminary Results on MCF-7.

We tested MCF-7 after in-flow compression to verify if possible passive intracellular delivery transports occur across the plasma membrane. We decided to load a 200 nm NPs solution in contact with the cell sample both at CTRL and PEO 09 conditions, in order to estimate whether there is the presence of an enhanced mechanism of NPs entry. In fact, we hypothesize that localized cell plasma membrane ruptures occur after the in-flow compression leading to enhanced NPs delivery. To proof it, we decided to test the NPs entry in freezing conditions, placing cells at 4° degrees at CTRL and after applied compression. At this temperature, the active mechanisms normally deputed to incorporate NPs are hindered [84]. As result, we observe that a passive movement of NPs is favoured at PEO 09 leading to a high delivery efficiency into treated cells (Fig. 27a-200nm and b). Furthermore, counting NP aggregates allows us to appreciate a 6-fold

increase of delivery at PEO 09 thanks to the passive passage across the ruptured plasma membrane (Fig. 27c). However, we also tested 1 µm particles in order to understand if a cut-off level is present in our delivery approach. Thus, at CTRL and PEO 09, we present interesting results about a 3-fold increase of particle entry (1 particle *per* cell) after in-flow compression, which suggests that the efficiency obviously reduces since a possible cut-off is reached, due to the high particle dimension (Fig. 27a-1µm and d).
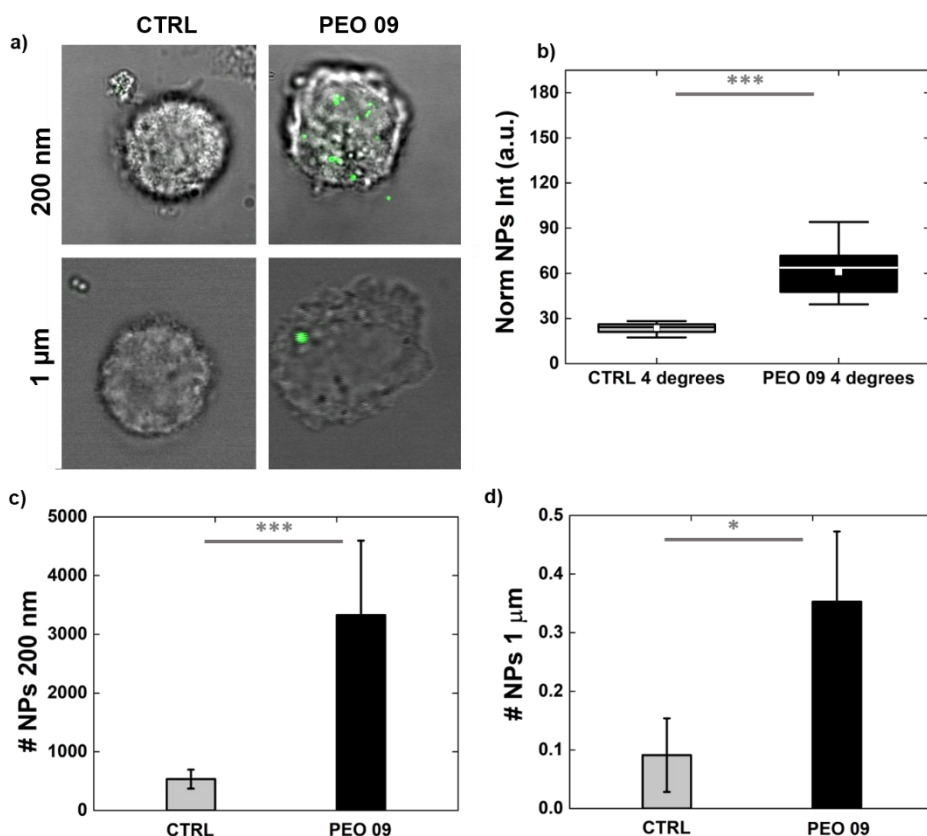

Fig. 27 NPs (200 nm and 1 µm) intracellular delivery into MCF-7. a) Confocal image of MCF-7 at CTRL and PEO 09 after NPs (green) intracellular delivery in freezing conditions. Evident enhanced delivery is appreciable in 200 nm entry after in-flow compression. With 1 µm particles, only one per cell are detected in our images. b) The normalized intensity of the NPs signal is reported for 200 nm NPs at the two experimental conditions. An overall increase of the intensity is appreciable at PEO 09 with

respect to CTRL. c) Counting NPs of 200 nm leading us to quantify the mean number of nanoparticles and aggregates that are present inside cells before and after the in-flow compression (CTRL n= 18; PEO 09 n=15). d) Counting of 1 μm particles inside cells is reported. Since the intracellular delivery provides an efficiency of one particle per cell, the reported data indicate the mean number of cells where a particle has been found that can be regarded as a percentage of cells where the delivery occurred, as well (CTRL n= 22; PEO 09 n=17). (*$p<0.05$; ***$p<0.001$).

Future perspectives of our research work consider to deeply investigate the possibility to further improve the microfluidic device for passive intracellular delivery. Investigations about plasma membrane recovery mechanisms after the applied in-flow compression as well as changes in NPs characteristics (e.g. external charge, stiffness, dimension) will be of fundamental interest for a device optimization and improvement. In fact, the implementation of the microfluidic device with other components (e.g. external electrical stimulation) can be addressed in order to create a comprehensive platform for cell diagnosis and drug delivery applications. Moreover, cells derived from non-solid tumours (i.e., blood cancer cells) will be analysed in order to understand how passive mechanisms of intracellular delivery can be induced to perform blood cell diagnosis and therapy.

Author contribution

M.I.M conceived the experimental design, conducted experiments, data analysis, and wrote the manuscript. Both the tutor and the scientific committee actively participated to the work during all of the three years, providing theoretical and practical guidance.
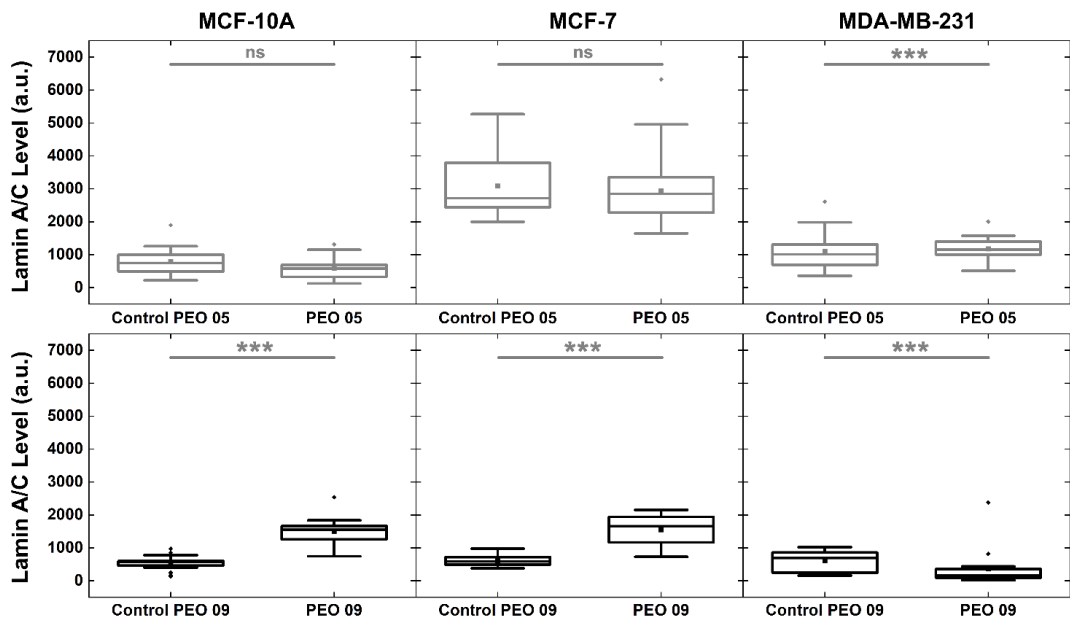
Appendix A

Fig. 1 Lamin A/C variation in terms of intensity level at the two different experimental conditions. On the top, data box chart to compare the Control condition at PEO 05 and the relative effect after the inflow compression. On the bottom, same aforementioned comparison at PEO 09 is presented. Statistical analysis has been performed by applying a Kruskal-Wallis test (ns $p > 0.05$; ***$p < 0.001$).
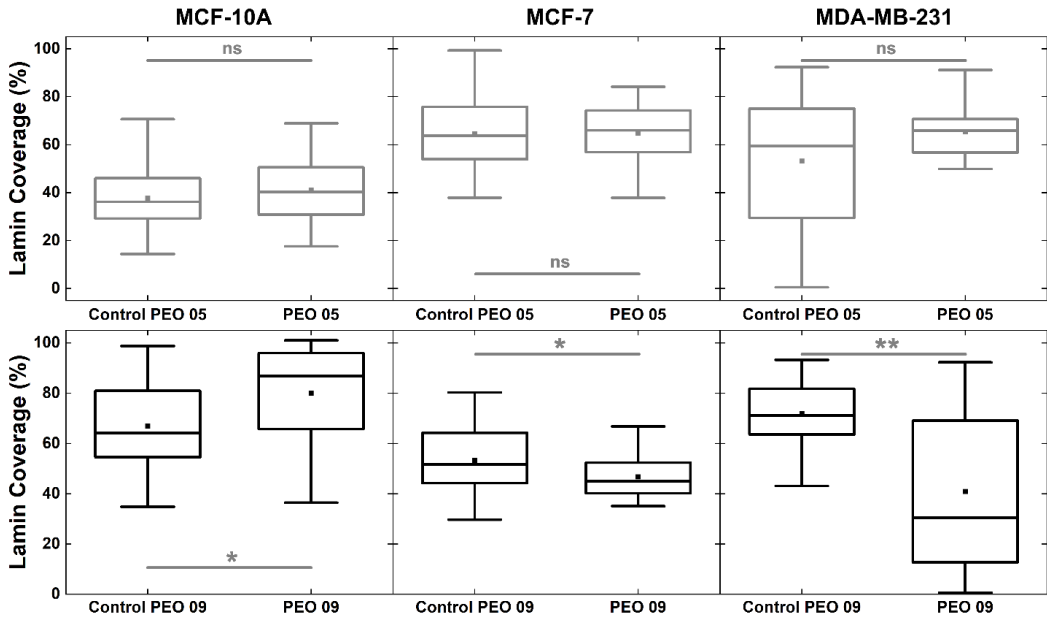
Fig. 2 Lamin A/C coverage changes at the two different experimental conditions. On the top, data box chart to compare the Control condition at PEO 05 and the relative effect after the in-flow compression. On the bottom, same aforementioned comparison at PEO 09 is presented. Statistical analysis has been performed by applying a Kruskal-Wallis test (ns $p > 0.05$; *$p < 0.05$; **$p<0.01$).
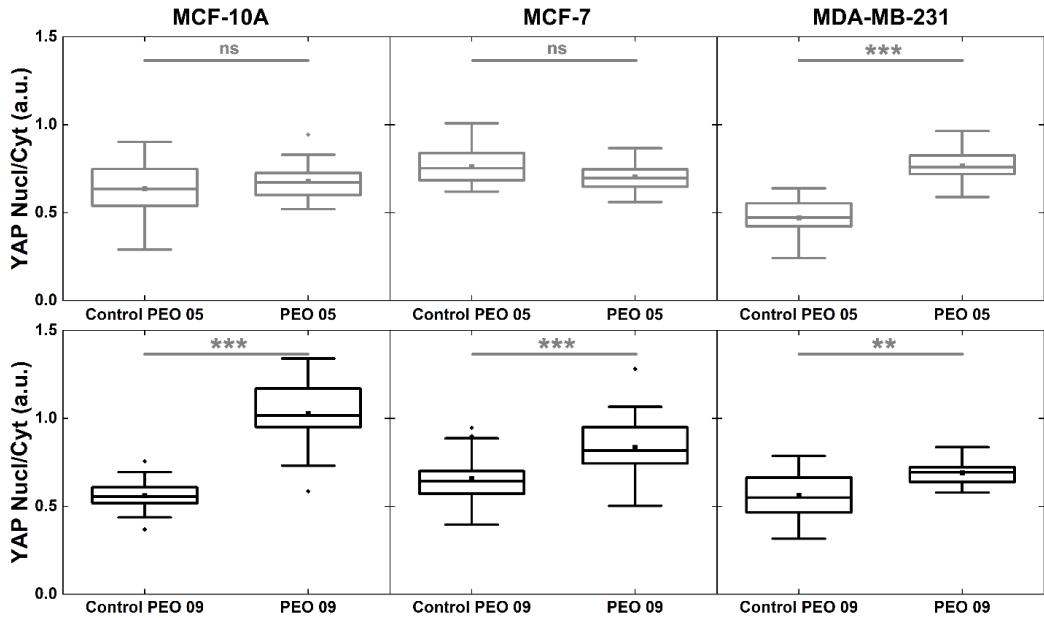
Fig. 3 YAP Nucl/Cyt ratio variation at the two different experimental conditions. On the top, data box chart to compare the Control condition at PEO 05 and the relative effect after the in-flow compression. On the bottom, same aforementioned comparison at PEO 09 is presented. Statistical analysis has been performed by applying a Kruskal-Wallis test (ns p > 0.05; **p<0.01; ***p<0.001).
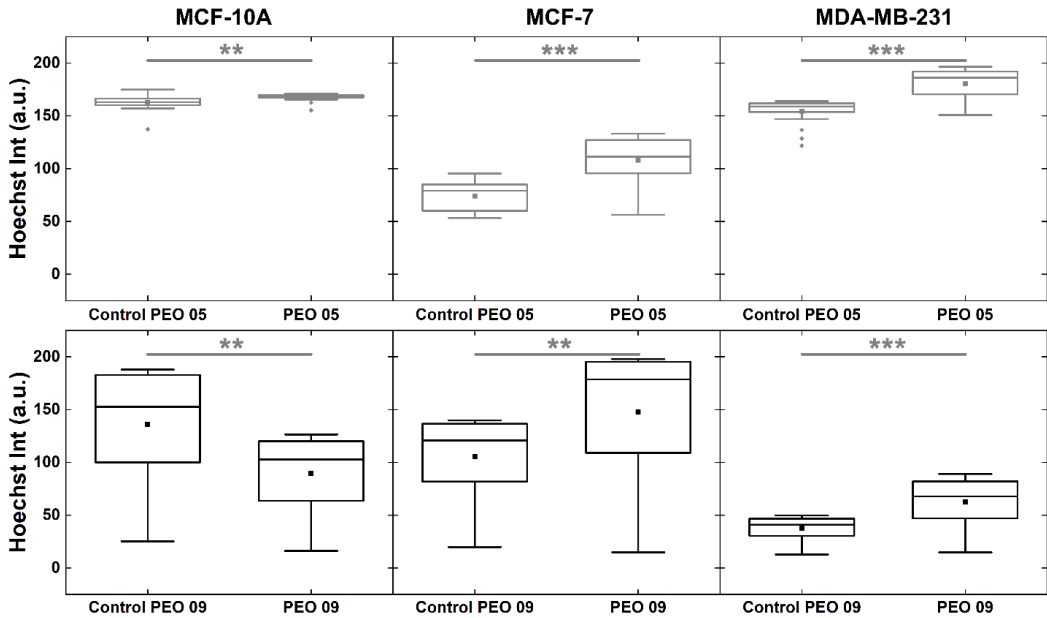
Fig. 4 Hoechst intensity variation at 300s of the total 600s of measurement for entry dynamic experiment. On the top, data box chart to compare the Control condition at PEO 05 and the relative effect after the in-flow compression. On the bottom, same aforementioned comparison at PEO 09 is presented. Statistical analysis has been performed by applying a Kruskal-Wallis test (**p<0.01; ***p<0.001).
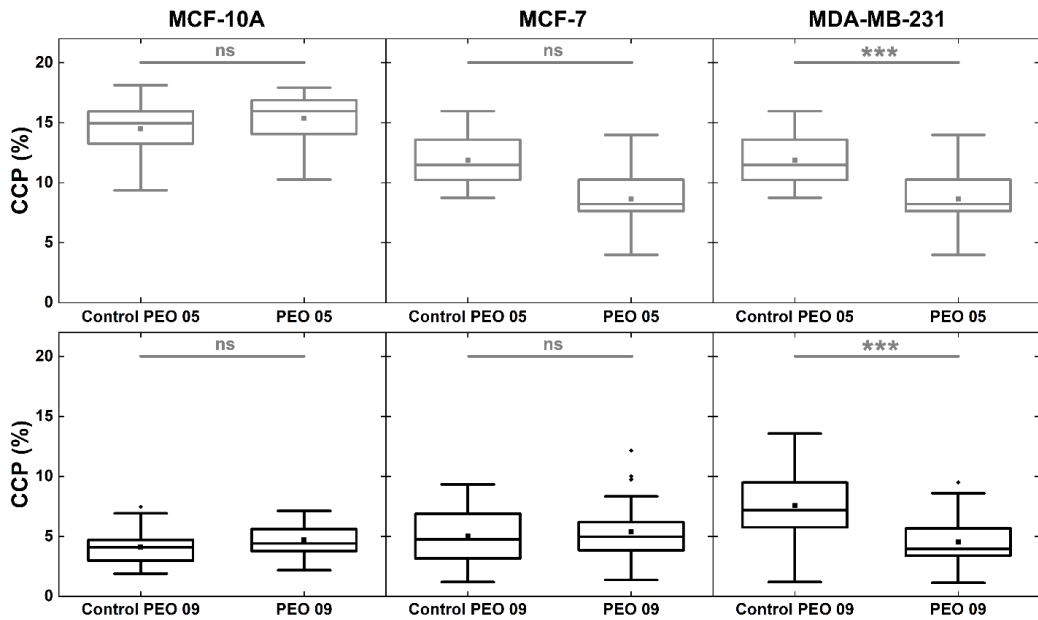
Fig. 5 Chromatin condensation (CCP) measurement at the two experimental conditions. On the top, data box chart to compare the Control condition at PEO 05 and the relative effect after the in-flow compression. On the bottom, same aforementioned comparison at PEO 09 is presented. Statistical analysis has been performed by applying a Kruskal-Wallis test (ns>0.05; ***p<0.001).
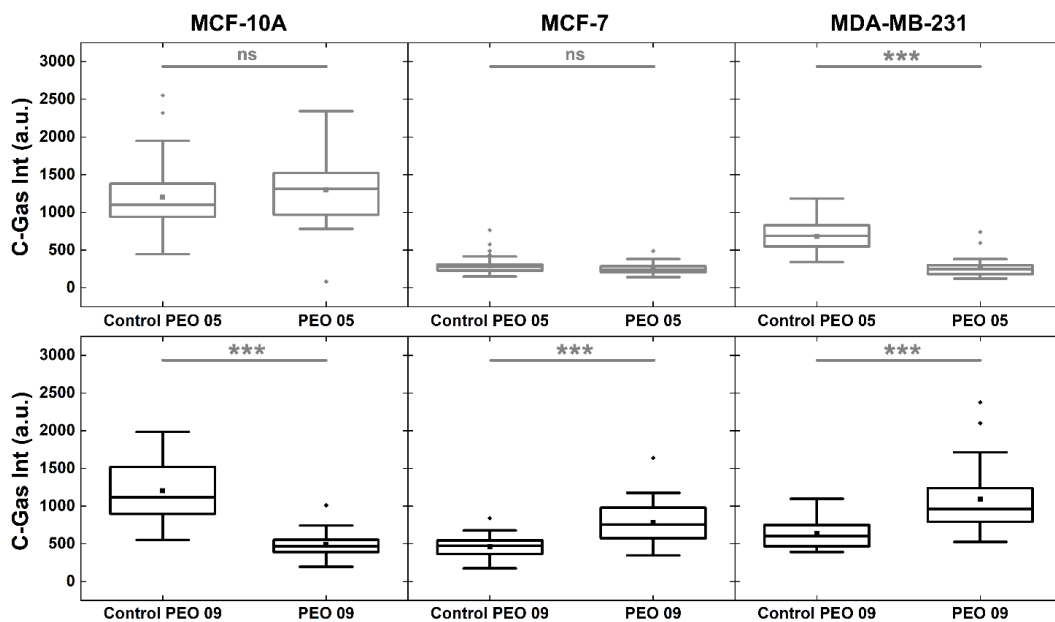
Fig. 6 cGAS intensity and activity into the cell cytoplasm. On the top, data box chart to compare the Control condition at PEO 05 and the relative effect after the in-flow compression. On the bottom, same aforementioned comparison at PEO 09 is presented. Statistical analysis has been performed by applying a Kruskal-Wallis test (ns>0.05; ***p<0.001).

Table 5 Statistical analysis of actin cortex and microtubule network intensity data. ns p > 0.05; * p < 0.05; **p<0.01; ***p<0.001.

	MCF-10 A	MCF-7	MDA-MB-231
CTRL with CTRLCYTD			
ACTIN	***	***	***
MT	***	***	**
CTRL with CTRLNOCO			
ACTIN	***	*	***
MT	***	***	***
CTRLCYTD with CTRLNOCO			
ACTIN	***	***	ns
MT	***	***	***
CTRL with PEO 09			
ACTIN	ns	*	***
MT	***	ns	***
CTRLCYTD with PEO 09 CYTD			
ACTIN	***	***	ns
MT	***	**	ns
CTRLNOCO with PEO 09 NOCO			
ACTIN	*	***	***
MT	*	*	ns

Table 6 Statistical analysis of actin cortex fragments position data. ns p > 0.05; * p < 0.05; **p<0.01; ***p<0.001.

	MCF-10 A	MCF-7	MDA-MB-231
CTRL with CTRLCYTD	***	***	***
CTRL with CTRLNOCO	***	**	***
CTRLCYTD with CTRLNOCO	***	***	***
CTRL with PEO 09	**	*	***
CTRLCYTD with PEO 09 CYTD	***	***	**
CTRLNOCO with PEO 09 NOCO	ns	ns	**

Table 7 Statistical analysis of actin cortex fragments area data. ns p > 0.05; * p < 0.05; **p<0.01; ***p<0.001.

	MCF-10 A	MCF-7	MDA-MB-231
CTRL with CTRL CYTD	*	***	ns
CTRL with CTRLNOCO	ns	ns	***
CTRLCYTD with CTRLNOCO	ns	***	**
CTRL with PEO 09	ns	ns	*
CTRL with PEO 05	***	***	*
CTRLCYTD with PEO 09 CYTD	Ns	ns	ns
CTRLNOCO with PEO 09 NOCO	ns	ns	ns

Appendix B

ImageJ Macro (MCF-10A and MCF-7 example) for actin cortex fragments analysis.

```
run ("Duplicate...", "title=[Image double.tif] channels=1");

run ("Duplicate...", " ");

run ("Threshold...");

setThreshold (65, 255);

setOption ("BlackBackground", false);

run ("Convert to Mask");

run ("Despeckle");

run ("Analyze Particles...", "add");

selectWindow ("Image double.tif");

roiManager ("Measure");
```

ImageJ Macro (MDA-MB-231 example) for actin cortex fragments analysis.

```
run ("Duplicate...", "title=[Image double.tif] channels=1");

run ("Duplicate...", " ");

run ("Threshold...");

setThreshold (100, 255);
```

setOption ("BlackBackground", false);

run ("Convert to Mask");

run ("Despeckle");

run ("Analyze Particles...", "add");

selectWindow ("Image double.tif");

roiManager ("Measure");

Then, once area and centroid coordinates are collected, an histogram analysis is proposed.

The threshold value has been fixed in order to remove possible noise or not specific signal points, collecting only constituents fragments of interest. Such value is cell line dependent.

References

[1] Lim CT, Bershadsky A, Sheetz MP. Mechanobiology, J R Soc Interface, 2010, 7-Suppl 3:S291-3.

[2] Maurer M, Lammerding J. The Driving Force: Nuclear Mechanotransduction in Cellular Function, Fate, and Disease, Annu Rev Biomed Eng., 2019,21:443-468.

[3] Di Carlo D., A mechanical biomarker of cell state in medicine, J Lab Autom., 2012, 17(1):32-42.

[4] Subra Suresh. Biomechanics and biophysics of cancer cells. Acta Materialia, 55(12):3989 – 4014, 2007.

[5] Janmey P. & Schmidt C., Experimental measurements of intracellular mechanics, in 'Cytoskeletal Mechanics: Models and Measurements in Cell Mechanics', Cambridge Texts in Biomedical Engineering, pp. 18-49.

[6] Jung W, Li J, Chaudhuri O, Kim T. Nonlinear Elastic and Inelastic Properties of Cells. J Biomech Eng. 2020 Oct 1;142(10):100806. doi: 10.1115/1.4046863.

[7] Nematbakhsh, Y., Pang, K.T. & Lim., C.T. Correlating the viscoelasticity of breast cancer cells with their malignancy. Convergent Sci. Phys.l Oncol. 3, 034003, 2017.

[8] Kim DH, Wong PK, Park J, Levchenko A, Sun Y., Microengineered platforms for cell mechanobiology, Annu Rev Biomed Eng., 2009,11:203-33.

[9] Nyberg KD, Hu KH, Kleinman SH, Khismatullin DB, Butte MJ, Rowat AC. Quantitative Deformability Cytometry: Rapid, Calibrated Measurements of Cell Mechanical Properties. Biophys J. 2017 Oct 3;113(7):1574-1584.

[10] P. M. Davidson and J. Lammerding, Trends Cell Biol., 2014, 24, 247-256.

[11] T. Harada, J. Swift, J. Irianto, J. W. Shin, K. R. Spinler, A. Athirasala, R. Diegmiller, P. C. D. P. Dingal, I. L. Ivanovska and D. E. Discher, J. Cell Biol., 2014, 204, 669-682.

[12] A. C. Rowat, D. E. Jaalouk, M. Zwerger, W. L. Ung, I. A. Eydelnant, D. E. Olins, A. L. Olins, H. Herrmann, D. A. Weitz and J. Lammerding, J. Biol. Chem., 2013, 288, 8610-8618.

[13] G. Xie, R. R. Walker and J. Irianto, Mutat. Res., Fundam. Mol. Mech. Mutagen., 2020, 821, 111717.

[14] A. Buxboim, J. Swift, J. Irianto, K. R. Spinler, P. C. Dave, P. Dingal, A. Athirasala, Y. R. C. Kao, S. Cho, T. Harada, J. W. Shin and D. E. Discher, Curr. Biol., 2014, 24, 1909-1917.

[15] X. Ding, M. P. Stewart, A. Sharei, J. C. Weaver, R. S. Langer and K. F. Jensen, Nat. Biomed. Eng., 2017, 1, 1-7.

[16] S. Dupont, L. Morsut, M. Aragona, E. Enzo, S. Giulitti, M. Cordenonsi, F. Zanconato, J. Le Digabel, M. Forcato, S. Bicciato, N Elvassore and S. Piccolo, Nature, 2011, 474, 179-183.

[17] C. M. Denais, R. M. Gilbert, P. Isermann, A. L. McGregor, M. te Lindert, B. Weigelin, P. M. Davidson, P. Friedl, K. Wolf and J. Lammerding, Science, 2016, 352, 353-358.

[18] F. Alisafaei, D. S. Jokhun, G. V. Shivashankar and V. B. Shenoy, PROC. NATL. ACAD. SCI. U. S. A., 2019, 116, 13200-13209.

[19] M. Raab, M. Gentili, H. de Belly, H. R. Thiam, P. Vargas, A. J. Jimenez, F. Lautenschlaeger, R. Voituriez, A. M. Lennon-Duménil, N. Manel and M. Piel, Science, 2016, 352, 359-362.

[20] Q. Zhang, A. C. Tamashunas, A. Agrawal, M. Torbati, A. Katiyar, R. B. Dickinson, J. Lammerding and T. P. Lele, Molecular Biology of the Cell, 2019, 30, 899-906.

[21] N. Dross, C. Spriet, M. Zwerger, G. Müller, W. Waldeck and J. Langowski, PLOS ONE, 2009, 4, 1-13.

[22] A. D. Stephens, E. J. Banigan, S. A. Adam, R. D. Goldman and J. F. Marko, Mol. Biol. Cell, 2017, 28, 1984-1996.

[23] A. Elosegui-Artola, I. Andreu, A. E. M. Beedle, A. Lezamiz, M. Uroz, A. J. Kosmalska, R. Oria, J. Z. Kechagia, P. Rico-Lastres, A. L. Le Roux, C. M. Shanahan, X. Trepat, D. Navajas, S. Garcia-Manyes and P. Roca-Cusachs, Cell, 2017, 171, 1397-1410.

[24] J. Dupire, M. Socol, and A. Viallat, Full dynamics of a red blood cell in shear flow, Proc. Natl. Acad. Sci. U. S. A., 2012, 109, 20808-20813.

[25] M. Urbanska, P. Rosendahl, M. Kraeter and J. Guck, High-throughput single-cell mechanical phenotyping with real-time deformability cytometry, In Methods in cell biology, Academic Press, 2018, 147, 175-198.

[26] C. Dupont, F. Delahaye, D. Barthès-Biesel and A-V. Salsac, Stable equilibrium configurations of an oblate capsule in simple shear flow, J. Fluid Mech., 2016, 791, 738-757.

[27] M. Abkarian, M. Faivre and A. Viallat, Swinging of red blood cells under shear flow. Phys. Rev. Lett., 2007, 98, 188302.

[28] C. Dupont, F. Delahaye, D. Barthès-Biesel and A-V. Salsac, Stable equilibrium configurations of an oblate capsule in simple shear flow, J. Fluid Mech., 2016, 791, 738-757.

[29] J. M. Skotheim and T. W. Secomb, Red blood cells and other nonspherical capsules in shear flow: Oscillatory dynamics and the tank-treading-to-tumbling transition, Phys. Rev. Lett., 98:078301, Feb 2007.

[30] X. Lu, L. Zhu, R-M. Hua and X. Xuan, Continuous sheath-free separation of particles by shape in viscoelastic fluids, Appl. Phys. Lett., 2015, 107, 264102.

[31] X. Lu and X. Xuan, Elasto-inertial pinched flow fractionation for continuous shape-based particle separation, Anal. Chem., 2015, 87, 11523-11530.

[32] Guck J, Schinkinger S, Lincoln B, Wottawah F, Ebert S, Romeyke M, Lenz D, Erickson HM, Ananthakrishnan R, Mitchell D, Käs J, Ulvick S, Bilby C. Optical deformability as an inherent cell marker for testing malignant transformation and metastatic competence. Biophys J. 2005 May;88(5):3689-98.

[33] Roth KB, Neeves KB, Squier J, Marr DW. High-throughput linear optical stretcher for mechanical characterization of blood cells. Cytometry A. 2016 Apr; 89(4):391-7.

[34] Gossett DR, Tse HT, Lee SA, Ying Y, Lindgren AG, Yang OO, Rao J, Clark AT, Di Carlo D. Hydrodynamic stretching of single cells for large population mechanical phenotyping. Proc Natl Acad Sci U S A. 2012 May 15;109(20):7630-5.

[35] Hur SC, Henderson-MacLennan NK, McCabe ER, Di Carlo D. Deformability-based cell classification and enrichment using inertial microfluidics. Lab Chip. 2011 Mar 7;11(5):912-20. doi: 10.1039/c0lc00595a. Epub 2011 Jan 27.

[36] Otto O, Rosendahl P, Mietke A, Golfier S, Herold C, Klaue D, Girardo S, Pagliara S, Ekpenyong A, Jacobi A, Wobus M, Töpfner N, Keyser UF, Mansfeld J, Fischer-Friedrich E, Guck J. Real-time deformability cytometry: on-the-fly cell mechanical phenotyping. Nat Methods. 2015 Mar;12(3):199-202, 4:202.

[37] B. Fregin, F. Czerwinski, D. Biedenweg, S. Girardo, S. Gross, K. Aurich and O. Otto, Nat. Commun. 2019, 10, 415.

[38] Deng, Y. et al. Inertial microfluidic cell stretcher (imcs): Fully automated, high-throughput, and near real-time cell mechanotyping. Small 13, 1700705, 2017.

[39] Hodgson, A. C., Verstreken, C. M., Fisher, C. L., Keyser, U. F., Pagliara, S., & Chalut, K. J. (2017). A microfluidic device for characterizing nuclear deformations. Lab on a Chip, 17(5), 805-813.

[40] Ito, H., & Kaneko, M. (2020). On-chip cell manipulation and applications to deformability measurements. ROBOMECH journal, 7(1), 1-11.

[41] M. J. Mitchell, C. Denais, M. F. Chan, Z. Wang, J. Lammerding and M. R. King, Am. J. Physiol., 2015, 309, C736-C746.

[42] M. Piergiovanni, V. Galli, G. Holzner, S. Stavrakis, A. DeMello and G. Dubini, Lab Chip, 2020, 20, 2539-2548.

[43] Yuan D, Zhao Q, Yan S, Tang SY, Alici G, Zhang J, Li W. Recent progress of particle migration in viscoelastic fluids. Lab Chip. 2018 Feb 13;18(4):551-567.

[44] D. Dannhauser, D. Rossi, F. Causa, P. Memmolo, A. Finizio, T. Wriedt, J. Hellmers, Y. Eremin, P. Ferraro and P. A. Netti, Optical signature of erythrocytes by light scattering in microfluidic flows, Lab Chip, 15, 3278-3285.

[45] Taesik Go, Hyeokjun Byeon, and Sang Joon Lee. Focusing and alignment of erythrocytes in a viscoelastic medium. Scientific reports, 7:41162, 2017.

[46] G. D'Avino, M. A. Hulsen, F. Greco and P. L. Maffettone, Numerical simulations on the dynamics of a spheroid in a viscoelastic liquid in a wide-slit microchannel, J. Non-Newtonian Fluid Mech., 2019, 263, 33-41.

[47] S. A. Abtahi and G. J. Elfring, Jeffery orbits in shear-thinning fluids, Phys. Fluids, 2019.

[48] Sung S. Lee, Yoonjae Yim, Kyung H. Ahn, and Seung J. Lee. Extensional flow-based assessment of red blood cell deformability using hyperbolic converging microchannel. Biomedical Microdevices, 11(5):1021, May 2009.

[49] Thomas J. Ober, Simon J. Haward, Christopher J. Pipe, Johannes Soulages, and Gareth H. McKinley. Microfluidic extensional rheometry using a hyperbolic contraction geometry. Rheologica Acta, 52(6):529–546, Jun 2013.

[50] Kai Kang, Kurt W. Koelling, and L. James Lee. Microdevice end pressure evaluations with bagley correction. Microfluidics and Nanofluidics, 2(3):223–235, May 2006.

[51] P.C. Sousa, P.M. Coelho, M.S.N. Oliveira, and M.A. Alves. Effect of the contraction ratio upon viscoelastic fluid flow in three-dimensional square contractions. Chemical Engineering Science, 66(5):998 – 1009, 2011.

[52] Henrik Bruus. Theoretical microfluidics, volume 18. Oxford university press Oxford, 2008.

[53] R. B. Bird, R. C. Armstrong and O. Hassager, Dynamics of polymeric liquids. Vol. 1: Fluid mechanics. Wiley-VCH Verlag GmbH & Co, Weinheim, Germany, 1987.

[54] A. Karnis and S. G. Mason, Particle motions in sheared suspensions. xix. viscoelastic media, Trans, Soc. Rheol., 1966, 10, 571-592.

[55] D. Di Carlo, Inertial microfluidics, Lab Chip, 2009, 9, 3038-3046.

[56] G. Romeo, G. D'Avino, F. Greco, P. A. Netti and P. L. Maffettone, Viscoelastic flow-focusing in microchannels: scaling properties of the particle radial distributions, Lab Chip, 13, 2802-2807.

[57] G. D'Avino, G. Romeo, M. M. Villone, F. Greco, P. A. Netti and P. L. Maffettone, Single line particle focusing induced by viscoelasticity of the suspending liquid: theory, experiments and simulations to design a micropipe flow-focuser, Lab Chip, 2012, 12, 1638-1645.

[58] B. P. Ho and L. G. Leal, Migration of rigid spheres in a two-dimensional unidirectional shear flow of a second-order fluid, J. Fluid Mech., 1976, 76, 783-799.

[59] F. Del Giudice, G. Romeo, G. D'Avino, F. Greco, P. A. Netti and P. L. Maffettone, Particle alignment in a viscoelastic liquid flowing in a square-shaped microchannel. Lab Chip, 2013, 13, 4263-4271.

[60] X. Lu, C. Liu, G. Hu and X. Xuan, Particle manipulations in non-newtonian microfluidics: A review, J. Colloid Interface Sci., 2017, 500, 182-201.

[61] G. B. Jeffery, The motion of ellipsoidal particles immersed in a viscous fluid, Proc. R. Soc. London, Ser. A, 1922, 102, 161-179.

[62] J. Irianto, D. A. Lee and M. M. Knight, Med. Eng. Phys., 2014, 36, 412-417.

[63] H. H. Hu and D. D. Joseph, Lift on a sphere near a plane wall in a second-order fluid, J. Non-Newtonian Fluid Mech., 1999, 88, 173-184.

[64] C. Rianna, M. Radmacher and S. Kumar, Direct evidence that tumor cells soften when navigating confined spaces, Mol. Biol. Cell, 2020, mbc-E19.

[65] G. I. Taylor, The motion of ellipsoidal particles in a viscous fluid, Proc. R. Soc. London, Ser. A, 1923, 103, 58-61.

[66] Chiotaki R, Polioudaki H, Theodoropoulos PA. Differential nuclear shape dynamics of invasive and non-invasive breast cancer cells are associated with actin cytoskeleton organization and stability. Biochem Cell Biol. 2014 Aug;92(4):287-95.

[67] J. Swift, I. L. Ivanovska, A. Buxboim, T. Harada, P. C. D. P. Dingal, J. Pinter, J. D. Pajerowski, K. R. Spinler, J. W. Shin, M. Tewari, F. Rehfeldt, D. W. Speicher and D. E. Discher. Science, 2013, 341, 6149.

[68] Xia, Yuntao, Charlotte R. Pfeifer, and Dennis E. Discher. "Nuclear mechanics during and after constricted migration." Acta Mechanica Sinica 35.2 (2019): 299-308.

[69] Zhang X. and Yonggang Lv. "Suspension state increases reattachment of breast cancer cells by up-regulating lamin A/C." Biochimica et Biophysica Acta (BBA)-Molecular Cell Research 1864.12 (2017): 2272-2282.

[70] I. Bronshtein, E. Kepten, I. Kanter, S. Berezin, M. Lindner, A. B. Redwood, S. Mai, S. Gonzalo, R. Foisner, Y. Shav-Tal and Y. Garini, Nat. Commun., 2015, 6, 8044.

[71] N. Zuleger, M. I. Robson and E. C. Schirmer, Nucleus, 2011, 2, 339-349.

[72] M. J. Puckelwartz, F. F. Depreux, E. M. McNally, Nucleus. 2011, 2, 162-7.

[73] N. Dross, C. Spriet, M. Zwerger, G. Müller, W. Waldeck and J. Langowski, PLOS ONE, 2009, 4, 1-13.

[74] Q. Chen, L. Sun, Z. J. Chen, Nat. Immunol., 2016, 17, 1142-9.

[75] H. Yang, H. Wang, J. Ren, Q. Chen and Z. J. Chen. PROC. NATL. ACAD. SCI. U. S. A., 2017, 114, E4612-E4620.

[76] Salbreux, G., Charras, G. & Paluch, E. Actin cortex mechanics and cellular morphogenesis. Trends Cell Biol. 22, 536-545, 2012.

[77] H Kubitschke et al 2017 New J. Phys. 19 093003.

[78] Ramdas, Nisha M., and G. V. Shivashankar. "Cytoskeletal control of nuclear morphology and chromatin organization." Journal of molecular biology 427.3 (2015): 695-706.

[79] Stewart, Martin P., Robert Langer, and Klavs F. Jensen. "Intracellular delivery by membrane disruption: mechanisms, strategies, and concepts." Chemical reviews 118.16 (2018): 7409-7531.

[80] Mellott, A. J.; Forrest, M. L.; Detamore, M. S. Physical Non-Viral Gene Delivery Methods for Tissue Engineering. Ann. Biomed. Eng. 2013, 41, 446−468.

[81] Lakshmanan, S.; Gupta, G. K.; Avci, P.; Chandran, R.; Sadasivam, M.; Jorge, A. E.; Hamblin, M. R. Physical Energy for Drug Delivery; Poration, Concentration and Activation. Adv. Drug Delivery Rev. 2014, 71, 98−114.

[82] McNeil, Paul L., and Richard A. Steinhardt. "Plasma membrane disruption: repair, prevention, adaptation." Annual review of cell and developmental biology 19.1 (2003): 697-731.

[83] Sharei A, Zoldan J, Adamo A, Sim WY, Cho N, Jackson E, Mao S, Schneider S, Han MJ, Lytton-Jean A, Basto PA, Jhunjhunwala S, Lee J, Heller DA, Kang JW, Hartoularos GC, Kim KS, Anderson DG, Langer R, Jensen KF. A vector-free microfluidic platform for intracellular delivery. Proc Natl Acad Sci U S A. 2013 Feb 5;110(6):2082-7.

[84] Monti DM, Guarnieri D, Napolitano G, Piccoli R, Netti P, Fusco S, Arciello A. Biocompatibility, uptake and endocytosis pathways of polystyrene nanoparticles in primary human renal epithelial cells. J Biotechnol. 2015 Jan 10;193:3-10.